

Çağlayan Aras

Anharmonic Free Energy Calculation
of Dynamically Unstable Crystal
Structures

Supervisors:

Prof. Dr. Jochen M. Schneider
Prof. Dr. Jörg Neugebauer
Dr. Moritz to Baben

Master of Science Thesis, Aachen, 10.09.2021

Contents

List of Figures	iii
List of Tables	v
1 Introduction	2
1.1 Motivation	2
1.2 Goal & Strategy	2
2 Theory	4
2.1 Thermodynamic Integration	5
2.1.1 Importance Sampling	5
2.1.2 Thermodynamic Integration	8
2.1.3 Thermodynamic Integration in Thermodynamics	11
2.1.4 Importance Sampling in Thermodynamics	13
2.1.5 Classical versus Quantum Partition Function	14
2.2 Harmonic Model	19
2.2.1 Double-well Potential	22
2.2.2 Temperature Dependent Effective Potential	23
2.2.3 High Displacement Model	24
2.3 Heat Capacity	25
2.4 Electronic Entropy	27
3 Results & Discussion	29
3.1 Titanium	29
3.2 Zirconium	33
3.3 Calcium	35
3.4 Al-Cu System	38

4 Conclusions	43
5 Declaration of Originality	45
Appendices	46
Appendix A Al-Cu System	46
References	48

List of Figures

1	Free energy surface of BCC Calcium.	4
2	Functions of IS example. Two different distributions are used as $q_0(x)$ and the results are compared to see the effects of weighting.	7
3	Running averages for different proposal distributions $p_0(x)$.	7
4	Another IS example with a different proposal distribution.	8
5	Intermediate functions between $q_0(x)$ and $q_1(x)$.	10
6	Thermodynamic integration.	11
7	Discrete energy states of quantum oscillator.	14
8	Classical and quantum partition function of a harmonic well.	15
9	Classical and quantum mechanical Helmholtz free energy of FCC Al.	16
10	Classical and quantum mechanical heat capacities.	16
11	Phonon dispersion of FCC Al.	17
12	Integrand of different harmonic bases.	18
13	Double-well potentials of BCC Zr. Red lines show the best fit of Equation (58) and dashed lines show the ideal harmonic wells.	22
14	Gibbs energy difference between BCC and HCP Zr.	22
15	Experimental and calculated phonon dispersion relations of BCC Zr and Ti. Experimental values of Zr[20] and Ti[21] are represented as black dots and the dashed lines between them are for the eye.	23
16	Phonon band structures of BCC Ti and Zr calculated with different finite displacements.	24
17	Electronic contributions to the heat capacities.	28
18	Gibbs energy difference between BCC and HCP Ti.	29
19	Integrand of Titanium.	30
20	Anharmonic and electronic entropies of titanium.	31

21	Enthalpy and entropy of transformation. Red dashed line shows the transformation temperature.	32
22	Heat capacity of titanium.	32
23	Integrands of Zirconium.	33
24	Free energies and heat capacities of zirconium.	34
25	Anharmonic and electronic entropies of zirconium.	34
26	Enthalpy and entropy of transformation. Red dashed line shows the transformation temperature.	34
27	Calculated and experimental heat capacity of calcium.	35
28	Integrands of Calcium.	36
29	Gibbs energy difference between BCC and FCC Ca.	36
30	Enthalpy and entropy of transformation. Red dashed line shows the transformation temperature.	37
31	Anharmonic and electronic entropies of calcium.	37
32	Al-Cu phase diagram from FScopp database.	38
33	Supercells used for Al-Cu system. Gray spheres represent Al atoms and brown spheres represent Cu atoms.	39
34	Birch-Murnaghan EOS of the Al-Cu supercells. From left to right, compositions are Cu, Al ₁ Cu ₉ and Al ₂₅ Cu ₇₅ .	40
35	Gibbs energy difference between BCC and FCC solutions at different chemical compositions.	41
36	Heat capacities of pure Al and Cu.	41
37	Anharmonic and electronic entropies of copper.	42
38	Al-Cu phase diagram with FCC, BCC and liquid phases only.	46
39	Integrands at ground state equilibrium volume.	47

List of Tables

1	Thermodynamic integration at 100K.	17
2	Thermodynamic integration at 500K.	19

Abstract

The Calphad method is a crucial tool for materials and industrial process design. Success of the method relies heavily on the quality of the materials data and preparation of the datasets requires a detailed and careful study. In this thesis, computational methods that calculate the finite temperature free energies of crystal structures are introduced and implemented on different phases of elements such as Ca, Ti, Zr, Al and Cu. The well known quasi-harmonic model cannot be applied to mechanically unstable phases such as BCC Al-Cu solution or BCC Ti because of the observed imaginary phonon frequencies. For such kind of phases, soft phonon modes are stabilized by selecting a value of finite displacement that is comparable to the desired temperature. Force constants obtained from such displacements are then used in the reference state of the Thermodynamic Integration (TI) method and anharmonic free energies are approximated. A detailed derivation of thermodynamic integration is provided in order to show the possible pitfalls to the reader. If the true form of the Gibbs free energy curve is known, heat capacity can be easily derived. However, small deviations in the free energy can lead to erroneous results. In addition to thermodynamic integration, alternative statistical models that estimate the pressure and volume dependent anharmonic heat capacities are presented.

Unary datasets are the foundation of many multi-component databases and require a critical assessment. Among these, a special attention should be given to energetically unfavourable end-members due to the limited amount of experimental data available. In literature, there exist two distinct heat capacity measurements for pure BCC Calcium. Grabowski et al. (2011) have already shown that the SGTE (Scientific Group Thermodata Europe) unary dataset is not the best selection according to DFT calculations. In this study, this is verified by using empirical potentials. At elevated temperatures, BCC Al-Cu solution is stable at around \sim 60-80 at.% Cu. In addition to the unary systems, it is also shown that for the Al-Cu system, the BCC solid solution phase is more stable than the FCC phase at elevated temperatures.

1 Introduction

All models are wrong, but some are useful.

George Box, 1976

1.1 Motivation

Assessment of thermodynamic data has a place in the very core of materials science. As a result of increasing computational power and resources, there is a substantial interest in using physical models. Harmonic model and quasi-harmonic approximation are pretty much the standard way of calculating finite temperature free energies of crystal structures and large ab-initio databases are published[1, 2]. However, many technologically important materials appear to be in phases that show dynamical instabilities. Examples can be found in shape memory alloys, ferroelectric, refractory and structural materials[3]. Thus, free energy calculation of dynamically unstable phases have critical importance. Phases stable at high temperatures such as BCC Ti, Zr or Ca exhibit imaginary phonon frequencies and harmonic models cannot be used to obtain their thermodynamic properties.

1.2 Goal & Strategy

Anharmonic free energy calculations require molecular dynamics (or Monte Carlo) sampling and computationally demanding. The aim of this thesis is not to provide the most reliable set of results, but to provide a benchmark model for dynamically unstable phases. As a result, empirical potentials from OpenKIM repository[4] are used and no DFT calculation is provided. The fundamental task of the thesis is to approximate the partition function of a canonical (NVT) ensemble which is computationally intractable. Thermodynamic Integration using Langevin Dynamics (TILD) is broadly used for this purpose. As is also the case for entropy, thermodynamic integration does not exclusively relate to thermodynamics,

but is instead part of a bigger picture. In Bayesian literature, it is used for approximating intractable marginal likelihood as well as for model selection. I will use thermodynamic integration to take the integral of a Gaussian function as an example throughout the derivation in Chapter 2.1. All physics related calculations are done within the pyiron⁵ framework which is integrated with LAMMPS⁶ and phonopy⁷. Relevant code can be found in my Github repository¹.

Last but not least, a scientist does not just sort of fit something. Every model comes with its own set of assumptions and we have responsibility on what we can and cannot infer from data and models. The theory section is therefore of great importance.

¹https://github.com/caglayanoaras/pyiron_examples

2 Theory

For each of the considered phases, there exists a Helmholtz free energy surface $F(V, T)$. Even though the experiments are generally performed at constant pressures, it is more convenient to approximate the Helmholtz free energy of a phase at a given temperature T and volume V . Once $F(V, T)$ is known, the Gibbs free energy surface can be calculated by performing a Legendre transformation. Harmonic model provides the free energy $F(T)$ at a given volume V and quasi-harmonic model is a construction of $F(V, T)$ by calculating $F(T)$ at different volumes using the harmonic model. Anharmonic free energies are assumed to be similar to what quasi-harmonic model provides. However, recent studies show that anharmonic contributions can change thermodynamic quantities both qualitatively and quantitatively[8]. Thermodynamic integration is a sampling method and it requires a reference base in which free energy is known. Therefore, quasi-harmonic calculations are required in order to estimate anharmonic free energies with TILD approach. For dynamically unstable phases, there exists no quasi-harmonic surface $F(V, T)$ under the assumption of small displacements and modifications have to be made.

Harmonic models have been extensively studied in literature and therefore it is only briefly reviewed in the second section. Ackland proposed a double well potential fitting approach for dynamically unstable phases[9]. Hellman et al. proposed temperature dependent effective potential (TDEP) method[10]. Influenced by these, a high displacement quasi-harmonic base is proposed for TILD model in this study.

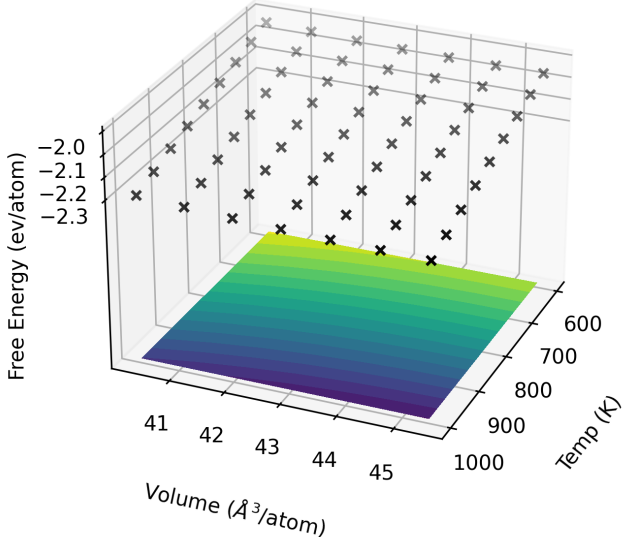


Figure 1: Free energy surface of BCC Calcium.

In the first section, a detailed derivation of thermodynamic integration and free energy perturbation theory is provided. An alternative model for heat capacity calculation is introduced in section 3. Due to the lack of electronic contributions, it is observed that simulations are underestimating heat capacities and entropies. Electronic contributions are discussed in section 4.

2.1 Thermodynamic Integration

2.1.1 Importance Sampling

To be able to understand thermodynamic integration, it is essential to understand importance sampling. Consider two probability distributions

$$p_1(x) = \frac{q_1(x)}{Z_1}, \quad (1)$$

$$p_0(x) = \frac{q_0(x)}{Z_0}. \quad (2)$$

$p_1(x)$ is a target distribution where $q_1(x)$ is known, but the normalization constant Z_1 is computationally intractable. The main idea of importance sampling (IS) is to estimate expectations $E_{p_1}(f(x))$ by using weighted samples from a tractable IS distribution $q_0(x)$. Unlike some other Monte Carlo methods, the goal here is not directly producing samples but to estimate expected values using weighted samples. The expected value of a random variable can be considered as an integral and therefore importance sampling is used for estimating the normalization constant Z_1 . Z_1 can be written as:

$$Z_1 = \int q_1(x)dx, \quad (3)$$

$$Z_1 = \int \frac{q_1(x)}{p_0(x)} p_0(x)dx, \quad (4)$$

$$Z_1 = \int Z_0 \frac{q_1(x)}{q_0(x)} p_0(x)dx. \quad (5)$$

As a result of Equation (5),

$$Z_1 = Z_0 \left\langle \frac{q_1(x)}{q_0(x)} \right\rangle_{p_0(x)} \quad (6)$$

or

$$\frac{Z_1}{Z_0} \approx \frac{1}{N} \sum_{n=1}^N \frac{q_1(x_n)}{q_0(x_n)}, \quad (7)$$

where $x_1, x_2, \dots, x_n \sim p_0(x)$.

One can estimate Z_1 using Equation (7), if $q_1(x)$ is known. Since we define $q_0(x)$, we already know Z_0 and $p_0(x)$. One possible option is to select $q_0(x)$ as a uniform distribution. In the following part, how $q_0(x)$ affects the result is explained.

Let's define $\frac{q_1(x)}{q_0(x)}$ as $w(x)$ and re-write Equation (7),

$$\bar{w} \approx \frac{1}{N} \sum_{n=1}^N w(x_n) \quad (8)$$

where $x_n \sim p_0(x)$.

The law of large numbers states that

$$\lim_{N \rightarrow +\infty} \bar{w} = \langle w(x) \rangle. \quad (9)$$

$\langle w(x) \rangle$ is not a random variable. It is a real number. However, \bar{w} is a random variable. The critical question is, what is the variance of \bar{w} ? The central limit theorem states that

$$\bar{w}_N \sim \mathcal{N} \left(\bar{w}_N | \mathbb{E}[w(x)], \frac{\text{Var}[w(x)]}{N} \right). \quad (10)$$

The variance of the normal distribution is

$$\text{Var}[\bar{w}] = \frac{\text{Var}[w(x)]}{N} \quad (11)$$

or

$$\text{Var}[\bar{w}] = \frac{1}{N} \left(\langle w(x)^2 \rangle_{p_0(x)} - \left(\frac{Z_1}{Z_0} \right)^2 \right). \quad (12)$$

The variance of \bar{w} depends on N and $p_0(x)$. Therefore, selection of $p_0(x)$ will affect the standard deviation of the estimate. It is also clear that the number of samples, N should be large for a smaller standard deviation.

As an example let's define a Gaussian $q_1(x)$ within an interval of $[-16, 16]$. We know the Gaussian function but we don't know the area beneath it (Z_1). Let's also define two different $q_0(x)$ functions, one uniform and one Gaussian. In this case we know both the normalization constant and the function. Figure 2 shows these functions. Our aim is to calculate the area (Z_1) beneath the Gaussian function $q_1(x)$ using weighted samples (Equation (7)).

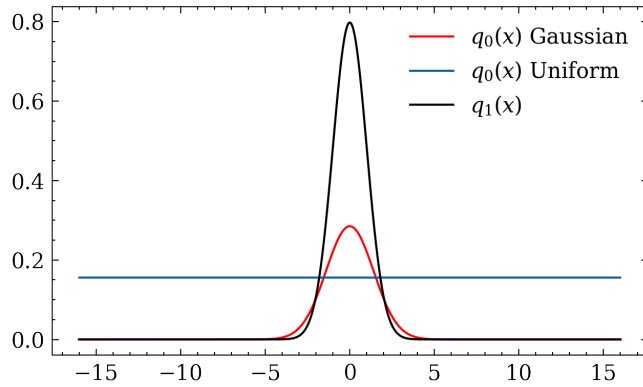


Figure 2: Functions of IS example. Two different distributions are used as $q_0(x)$ and the results are compared to see the effects of weighting.

Let's use Equation (7) and sample 1,2,3 ... 4000 variables from $p_0(x)$ in order to estimate Z_1 . Figure 3 shows the calculated Z_1 for both Gaussian and uniform $q_0(x)$.

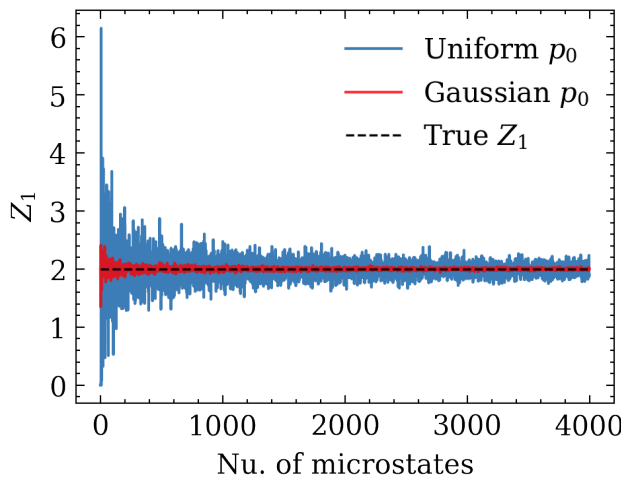


Figure 3: Running averages for different proposal distributions $p_0(x)$.

Figure 3 indicates that the variance of the result is indeed depends on N and $p_0(x)$. Depending on our choice of $p_0(x)$, it is possible to converge to the result quicker. However, our choice of $p_0(x)$ does not change the result. The result of the integral is a value and our aim is to estimate it as efficiently as possible.

2.1.2 Thermodynamic Integration

Now let's try to find the same Z_1 in our example but select another $q_0(x)$ function. Figure 4 shows the new Gaussian function and the calculated Z_1 for different number of samples.

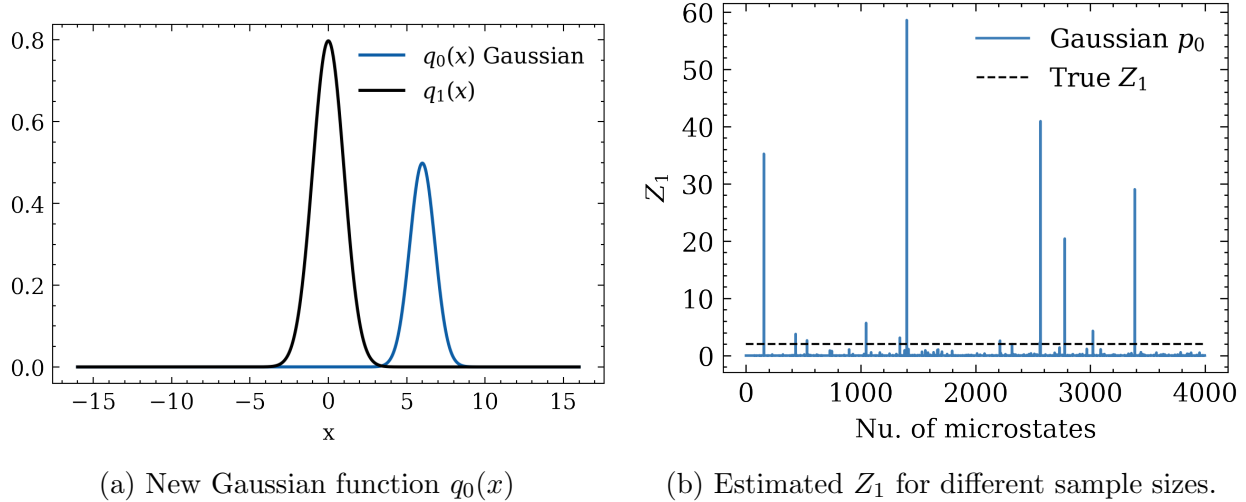


Figure 4: Another IS example with a different proposal distribution.

Figure 4b shows that the success of importance sampling depends on the selected $p_0(x)$. $q_0(x)$ and $q_1(x)$ were similar distributions in the first example (Figure 2) and in the last example these distributions are quite different. To overcome this, one can define intermediate steps and do importance sampling at each of these intermediate steps. Let's define intermediate steps as t_1, t_2, \dots, t_k . Normalization constants can be written as

$$\frac{Z_1}{Z_0} = \frac{Z_{t_1}}{Z_0} \frac{Z_{t_2}}{Z_{t_1}} \cdots \frac{Z_1}{Z_{t_k}} \quad (13)$$

or more conveniently

$$\log \frac{Z_1}{Z_0} = \log \frac{Z_{t_1}}{Z_0} + \log \frac{Z_{t_2}}{Z_{t_1}} + \dots + \log \frac{Z_1}{Z_{t_k}}. \quad (14)$$

We can write the intermediate steps as an integral

$$\log \frac{Z_{t_2}}{Z_{t_1}} = \int_{t_1}^{t_2} \frac{d}{dt} \log Z_t dt \quad (15)$$

where

$$p_t(x) = \frac{1}{Z_t} q_t(x). \quad (16)$$

Equation (15) can also be written as

$$\log \frac{Z_{t_2}}{Z_{t_1}} = \int_{t_1}^{t_2} \frac{1}{Z_t} \frac{d}{dt} Z_t dt. \quad (17)$$

Combining Equation (17) with Equation (16) yields

$$\log \frac{Z_{t_2}}{Z_{t_1}} = \int_{t_1}^{t_2} \int_x \frac{p_t(x)}{q_t(x)} \frac{d}{dt} q_t(x) dx dt \quad (18)$$

or

$$\log \frac{Z_{t_2}}{Z_{t_1}} = \int_{t_1}^{t_2} \left\langle \frac{d}{dt} \log q_t(x) \right\rangle_{p_t(x)} dt. \quad (19)$$

$q_t(x)$ is an intermediate function between $q_0(x)$ and $q_1(x)$. It is not unique and be our own choice. A convenient definition can be

$$q_t = q_0^{1-t} q_1^t. \quad (20)$$

Combining Equation (19) and Equation (20) will yield

$$\log \frac{Z_{t_2}}{Z_{t_1}} = \int_{t_1}^{t_2} \left\langle \frac{d}{dt} \log q_0^{1-t}(x) q_1^t(x) \right\rangle_{p_t(x)} dt \quad (21)$$

or

$$\log \frac{Z_{t_2}}{Z_{t_1}} = \int_{t_1}^{t_2} \left\langle \log \frac{q_1(x)}{q_0(x)} \right\rangle_{p_t(x)} dt. \quad (22)$$

Equation (22) is an intermediate step of Equation (14). Finally, by adding up these intermediate terms, Equation (14) can be written as

$$\log \frac{Z_1}{Z_0} = \int_0^1 \left\langle \log \frac{q_1(x)}{q_0(x)} \right\rangle_{p_t(x)} dt. \quad (23)$$

Equation (23) is the thermodynamic integration. In the following section, a specific form of this equation is used for physical systems. Let's go back to the example and define 51 t points so there will be 51 $q_t(x)$ functions (Equation (20)). All these functions are intermediate functions between $q_0(x)$ and $q_1(x)$ and plotted in Figure 5 as dashed lines. Note that $q_t(x)$ is always a Gaussian if $q_0(x)$ and $q_1(x)$ are Gaussians according to Equation (20).

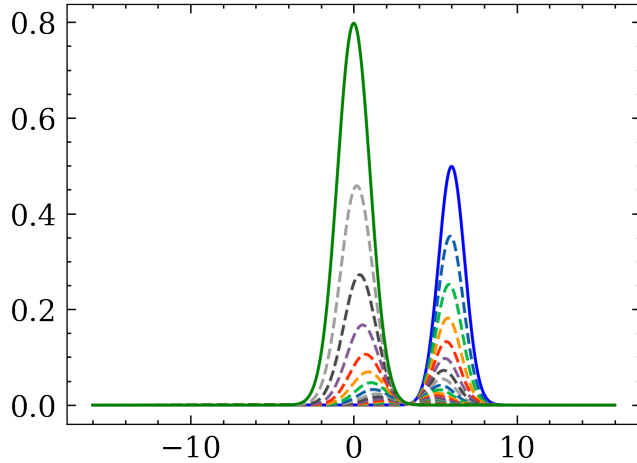


Figure 5: Intermediate functions between $q_0(x)$ and $q_1(x)$.

Sampling at each t value will provide us the integrand of Equation (23). Figure 6a shows how the integrand changes with t , where 4000 samples were used at each t to evaluate the expected value inside the integral. Now one can calculate the area, or normalization constant Z_1 . Figure 6b shows the number of samples used to approximate the integrand at each t value versus the calculated Z_1 . The value is around 2 as in the first example which is the true area of the Gaussian function $q_1(x)$.

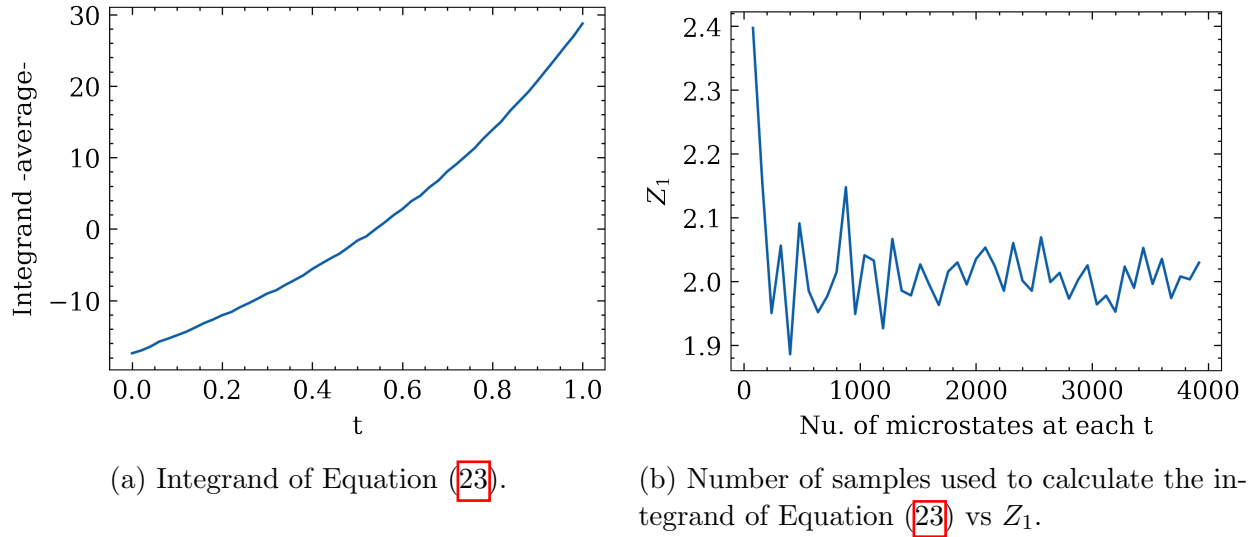


Figure 6: Thermodynamic integration.

In conclusion, what TI does is calculating the integrals or estimating expected values. The final result we get, Z_1 , is independent from the proposal distribution $p_0(x)$ and its normalizing constant Z_0 (or just $q_0(x)$). However, selection of $p_0(x)$ is critical because it will decide how many samples are needed in order to approximate the integral. The more similar $p_0(x)$ and $p_1(x)$, the better it is.

2.1.3 Thermodynamic Integration in Thermodynamics

In this chapter, the mathematical model derived in previous section is used to estimate the partition function of a canonical ensemble, which is basically a computationally intractable integral. In canonical ensemble, the probability of observing a microstate at a given temperature is

$$p_0(x) = \frac{e^{-\beta H_{0,x}}}{Z_0}, \quad (24)$$

$$p_1(x) = \frac{e^{-\beta H_{1,x}}}{Z_1}. \quad (25)$$

In this case let's assume that both proposal and target distributions obey the exponential rule

$$q_0(x) = e^{-\beta H_{0,x}} \text{ and } q_1(x) = e^{-\beta H_{1,x}}. \quad (26)$$

The partition function Z_1 can be written as an integral

$$Z_1 = \int e^{-\beta H_{1,x}} dx. \quad (27)$$

Once the partition function is known, one can get the Helmholtz free energy using the relation

$$A = -1/\beta \ln(Z). \quad (28)$$

Let's re-write equation (23) from Chapter 1

$$\log \frac{Z_1}{Z_0} = \int_0^1 \left\langle \log \frac{q_1(x)}{q_0(x)} \right\rangle_{p_t(x)} dt. \quad (29)$$

Combining it with Equation (28) and Equation (26) will yield

$$-\beta(A_1 - A_0) = -\beta \int_0^1 \langle H_{1,x} - H_{0,x} \rangle_{p_t(x)} dt \quad (30)$$

or

$$A_1 = A_0 + \int_0^1 \langle U_{1,x} - U_{0,x} \rangle_{p_t(x)} dt. \quad (31)$$

It is important to note that total energy H has changed to potential energy U . This is not going to make any difference. By looking at the Equation (29), one can easily see that the kinetic terms are canceling out. The $p_t(x)$ distribution in Equation (31) is clarified as follows

$$q_t(x) = e^{-\beta U_{0,x}(1-t)} + e^{-\beta U_{1,x}(t)}, \quad (32)$$

$$q_t(x) = e^{-\beta[(U_{1,x} - U_{0,x})t + U_{0,x}]}, \quad (33)$$

$$(U_{1,x} - U_{0,x})t + U_{0,x} = U_{\text{hybrid}}(t) = tU_{\text{anharmonic}} + (1-t)U_{\text{harmonic}}. \quad (34)$$

This concludes the derivation of Equation (35) which is frequently used in literature [11, 12, 13].

$$F_1(N, V, T) = F_0(N, V, T) + \int_0^1 \langle U_1 - U_0 \rangle_\lambda d\lambda \quad (35)$$

Langevin dynamics is used for sampling of canonical ensemble at any given intermediate step λ throughout this study. LAMMPS package as integrated into the pyiron framework is used for the simulations.

2.1.4 Importance Sampling in Thermodynamics

Exactly in the same manner as thermodynamic integration, the free energy perturbation (FEP) method [14] is used for approximating free energy differences. In this section, it is shown that FEP method is nothing but importance sampling. The equation used for the FEP method is

$$F_B(N, V, T) - F_A(N, V, T) = -k_B T \ln \left\langle \exp \left(-\frac{E_B - E_A}{k_B T} \right) \right\rangle_A. \quad (36)$$

Let's re-write the previously derived equation of importance sampling

$$Z_1 = Z_0 \left\langle \frac{q_1(x)}{q_0(x)} \right\rangle_{p_0(x)}. \quad (37)$$

Combining it with Equation (26) will yield

$$Z_1 = Z_0 \left\langle e^{-\beta(H_{1,x} - H_{0,x})} \right\rangle_{p_0(x)}. \quad (38)$$

Writing partition functions in terms of Helmholtz free energy yields

$$F_1 - F_0 = -k_B T \ln \left\langle \exp \left(-\frac{H_{1,x} - H_{0,x}}{k_B T} \right) \right\rangle_{p_0(x)}. \quad (39)$$

This concludes that the FEP method is just a specific form of importance sampling.

2.1.5 Classical versus Quantum Partition Function

Thermodynamic integration and free energy perturbation theory are explained from the classical statistical mechanics point of view in the previous chapters. However, for crystals, the classical partition function differs from the quantum mechanical one especially at low temperatures. In this section, this issue is addressed and an example of FCC aluminum is provided.

A phonon resides in a harmonic well (Figure 7) and the partition function of a single atom can either be calculated by discrete or continuous energy states. Calculating the reference free energy F_0 in Equation (35) with respect to the discrete energy states will bring mathematical inconsistencies, since Equation (26) is no more valid. In the following example of aluminum, F_0 is calculated with both classical and quantum mechanical oscillators and the results are interpreted.

Energy levels of a quantum harmonic oscillator are

$$E_n = \hbar\omega\left(n + \frac{1}{2}\right) \quad (40)$$

with integer quantum numbers. The partition function is

$$Z = \sum_{n=0}^{\infty} e^{-\beta E_n} = e^{-\frac{\beta\hbar\omega}{2}} \sum_{n=0}^{\infty} (e^{-\beta\hbar\omega})^n. \quad (41)$$

Since

$$\sum_{n=0}^{\infty} x^n = \frac{1}{1-x}, \quad (42)$$

The partition function of the quantum harmonic oscillator becomes

$$Z = \frac{e^{-\frac{\beta\hbar\omega}{2}}}{1 - e^{-\frac{\beta\hbar\omega}{2}}}. \quad (43)$$

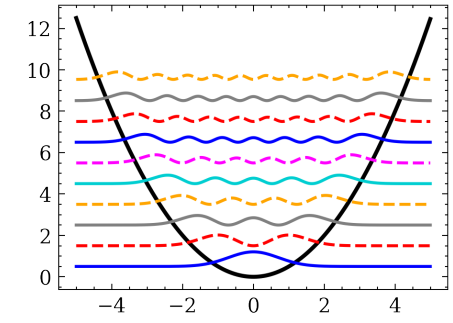


Figure 7: Discrete energy states of quantum oscillator.

Multiplying values of all reciprocal mesh will yield

$$Z = \prod_{\mathbf{q}\nu} \frac{\exp(-\hbar\omega(\mathbf{q}\nu)/2k_B T)}{1 - \exp(-\hbar\omega(\mathbf{q}\nu)/k_B T)}. \quad (44)$$

Equation (44) is used by the phonopy package in order to calculate the thermodynamic properties. Partition function of classical harmonic oscillator is

$$Z = \frac{1}{h} \int_{-\infty}^{\infty} \exp\left[-\frac{\beta}{2m} p^2\right] dp \int_{-\infty}^{\infty} \exp\left[-\frac{\beta}{2} m\omega^2 x^2\right] dx. \quad (45)$$

After doing the integrations it becomes

$$Z = \frac{1}{\beta\hbar\omega}. \quad (46)$$

Multiplication in reciprocal space will yield

$$Z = \prod_{\mathbf{q}\nu} \frac{1}{-\hbar\omega(\mathbf{q}\nu)/k_B T}. \quad (47)$$

Figure 8 shows how Equation (46) and Equation (43) change with respect to the $\beta\hbar\omega$ term.

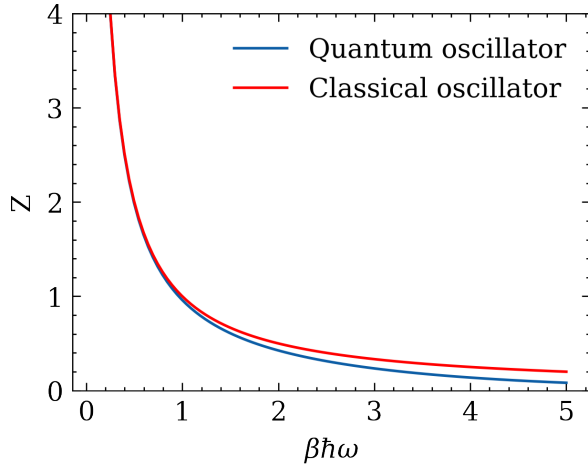


Figure 8: Classical and quantum partition function of a harmonic well.

The difference between the oscillators not only depends on the temperature but also the frequency of the harmonic well. As temperature increases and frequency decreases, the difference between the partition functions shrinks (Figure 8). The classical partition function is added to the phonopy package and the thermodynamic properties of FCC aluminum are calculated within the phonopy framework.

The integrand in Equation (35) is kept independent of the partition function being classical or quantum mechanical. However, the

reference free energies are different and this will affect the approximated anharmonic free energies. In order to calculate the classical and quantum reference free energies, force constant tensor of 108 atom FCC aluminum supercell is calculated with EAM potentials provided by Mishin et al.^[15] by a displacement of 0.01 Å.

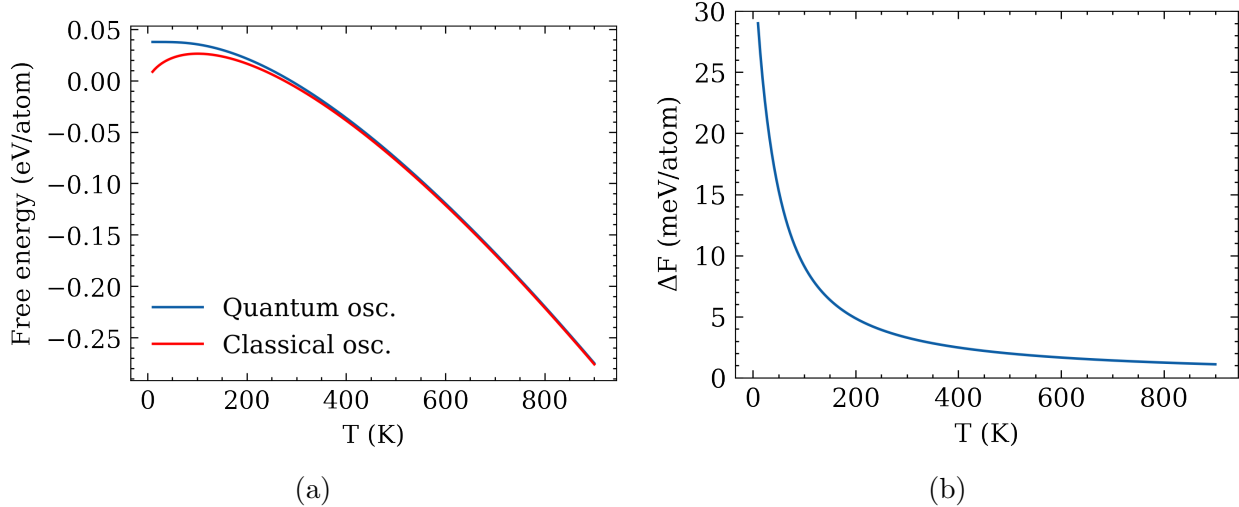


Figure 9: Classical and quantum mechanical Helmholtz free energy of FCC Al.

Figure 9b shows the free energy difference between the results calculated with different oscillators and even at high temperatures such as 900K, the difference is 1.1 meV. This situation is one of the many contributing factors to the uncertainty of the result and it should not be neglected considering that the reported uncertainties in literature are around 1 meV^[11].

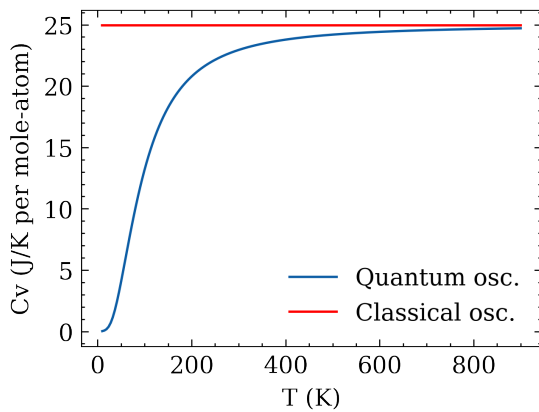


Figure 10: Classical and quantum mechanical heat capacities.

Figure 10 shows the heat capacities at constant volume calculated by phonopy both with continuous and discrete partition functions. Dulong-Petit law states that the molar heat capacity of an element is independent of temperature and is equal to $3R$ which is 24.94 J/K per mole-atom. Based on the previous chapters, it is straightforward to show that thermodynamic integration results should not depend on the force constants.

To prove this point, two sets of force constants are created for FCC Al. Force constants

are calculated using finite displacement method by displacing the atoms 0.01 and 0.6 Å. Additionally, force constants calculated by high displacement are arbitrarily multiplied with 1.5. Figure 11b shows the phonon dispersion relation for arbitrarily modified (stiffer) force

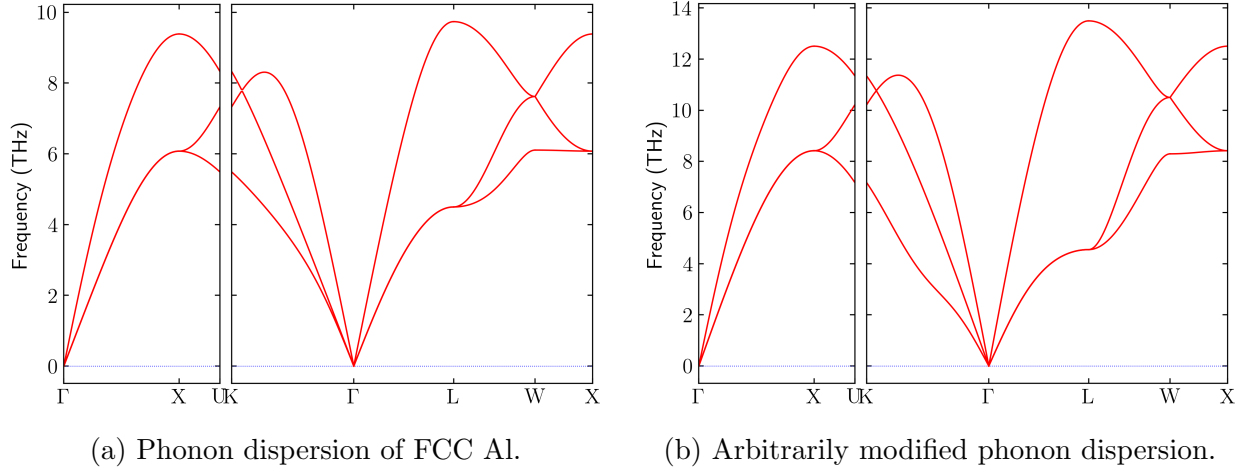


Figure 11: Phonon dispersion of FCC Al.

constants. Anharmonic free energy is calculated with respect to these two different harmonic basis at temperatures of 100 and 500 K. Results are shared in Table 1 and 2 respectively. Langevin dynamics simulations are performed with a sampling period of 25 fs at 32 λ points. For each λ point of 100 K simulation, 1940 microstates are sampled to ensure a standard error less than 1 meV on estimation of expected values. This number is 3940 for 500 K simulation. Figure 12 shows the integrand of normal and stiffer force constants both for 100 and 500 K simulations.

Table 1: Thermodynamic integration at 100K.

Classical	F_0	TILD Integral	FEP	TILD F_1	FEP F_1
Stiff	33.06 meV	-6.75 meV	-6.81 meV	26.31 meV	26.25 meV
Normal	26.15 meV	0.10 meV	0.10 meV	26.25 meV	26.25 meV
Quantized	F_0	TILD Integral	FEP	TILD F_1	FEP F_1
Stiff	48.61 meV	-6.75 meV	-6.81 meV	41.86 meV	41.80 meV
Normal	35.28 meV	0.10 meV	0.10 meV	35.38 meV	35.38 meV

Table 1 summarizes Equation (35) and Equation (36) for FCC Al at 100 K and results are

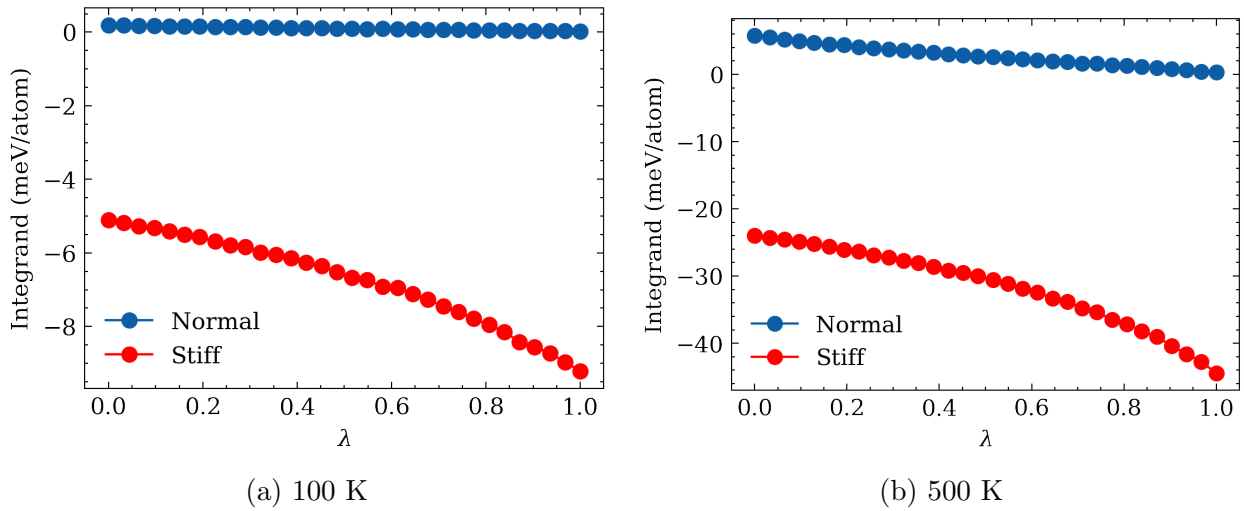


Figure 12: Integrands of different harmonic bases.

in agreement with the provided algebra. Anharmonic partition function, in other words the value of the intractable integral that needs to be approximated is independent of the reference selection. Both sets of force constants yield the same value that is 26.3 meV. This is the free energy according to classical mechanics. If basis free energy is calculated with respect to the quantized energy states, Equation (35) is no more valid and one ends up with final results that depend on the selected basis. The results, 41.86 meV and 35.38 meV are neither classical nor quantum mechanical free energies. However, ignoring this issue and naively taking the quantum mechanical quasi-harmonic free energy surface as a reference can be justified for dynamically stable phases. At low temperatures, atoms reside in a harmonic well and the integral will be close to zero since there is very little to none anharmonicity. Thus, one will obtain the quasi-harmonic free energy at low temperatures. At high temperatures, classical and quantum free energies are getting similar and the result of the thermodynamic integration will provide the classical anharmonic free energy. In between can be justified as an interpolation between classical and quantum mechanics. There exists no such option for dynamically unstable phases since there exists no quasi-harmonic surface. Table 2 shows the results for 500 K and just like in the 100 K case classical anharmonic free energies are similar for both sets of force constants.

In conclusion, TI and FEP models are classical models and are used for calculating the

integral in order to approximate the partition function. TI is a combination of intermediate FEP models and it is more advanced compared to FEP. An implementation of TILD model on low temperature simulations will bring mathematical inconsistencies due to the difference between classical and quantized partition functions.

Table 2: Thermodynamic integration at 500K.

Classical	F_0	TILD Integral	FEP	TILD F_1	FEP F_1
Stiff	-42.70 meV	-31.52 meV	-31.84 meV	-74.22 meV	-74.55 meV
Normal	-77.28 meV	2.75 meV	2.68 meV	-74.53 meV	-74.60 meV
Quantized	F_0	TILD Integral	FEP	TILD F_1	FEP F_1
Stiff	-39.12 meV	-31.52 meV	-31.51 meV	-70.64 meV	-70.63 meV
Normal	-75.29 meV	2.75 meV	2.76 meV	-72.54 meV	-72.53 meV

2.2 Harmonic Model

After demystifying TILD and FEP from statistics point of view, a discussion needs to be made about a proper selection of harmonic model of dynamically unstable phases. In this section, fundamentals of the harmonic model is shortly summarized first. Then, double well potentials and temperature dependent effective potential methods are reviewed. Finally, a finite displacement method with high displacement is proposed.

Born-Oppenheimer Hamiltonian for a set of N atoms can be written as

$$H(\{R_i\}, \{P_i\}) = \sum_{i=1}^{3N} \frac{P_i^2}{2M_i} + U(\{R_i\}). \quad (48)$$

The potential energy of interacting atoms can be represented as Taylor series around the equilibrium geometry. The series around the equilibrium R_i^0 yields

$$U(R_i) = U(R_i^0) + \left. \frac{\partial U(R_i)}{\partial R_i} \right|_{R_i^0} s_i + \frac{1}{2} \left. \frac{\partial^2 U(R_i)}{\partial R_i^2} \right|_{R_i^0} s_i^2 + \frac{1}{6} \left. \frac{\partial^3 U(R_i)}{\partial R_i^3} \right|_{R_i^0} s_i^3 + \dots, \quad (49)$$

where: $s_i = R_i - R_i^0$.

At point R_i^0 , first derivative vanishes since there exists no force at equilibrium. Neglecting third and higher terms will yield

$$U(R_i) \approx U(R_i^0) + \frac{1}{2} \frac{\partial^2 U(R_i)}{\partial R_i^2} \Big|_{R_i^0} s_i^2. \quad (50)$$

Writing Equation (50) for N atoms in three dimensions will lead to

$$H(\{R_i\}, \{P_i\}) = \sum_{i=1}^{3N} \frac{P_i^2}{2M_i} + U(\{R_i^0\}) + \frac{1}{2} \sum_{i,j}^{3N} \frac{\partial^2 U}{\partial R_i \partial R_j} \Big|_{\{R_i\}} s_i s_j. \quad (51)$$

Exploiting the crystal symmetry, Equation (51) can be written in a more compact form

$$H = \sum_{i,I}^{3N, N_{cell}} \frac{P_{i,I}^2}{2M_i} + U(\{R_{i,I}^0\}) + \frac{1}{2} \sum_{i,I,j,J}^{3N, N_{cell}} \frac{\partial^2 U}{\partial R_{i,I} \partial R_{j,J}} \Big|_{\{R_{i,I}^0\}} s_{i,I} s_{j,J} \quad (52)$$

where: N is the total number of atoms in the unit cell,

N_{cell} is the number of cells,

$R_{i,I}$ is position of i^{th} atom in I^{th} cell,

R_I is Bravais lattice site of I^{th} cell.

Accordingly, classical equations of motion for atoms can be written as

$$M_i \ddot{s}_{i,I} = \sum_{j,J}^{3N, N_{cell}} \frac{\partial^2 U}{\partial R_{i,I} \partial R_{j,J}} \Big|_{\{R_{i,I}^0\}} s_{j,J}. \quad (53)$$

Positions of the atoms have a harmonic time dependence and the dependence of the displacement of atoms from one unit cell to another is also harmonic. Therefore, an ansatz can be defined as

$$s_{i,I} = \frac{A_i e^{i(kR_I - wt)}}{\sqrt{M_i}}, \quad (54)$$

where A_i is a constant number that refers to the amplitude of each atom. Plugging Equation

(54) to Equation (53) will yield

$$w^2 A_i = \sum_j^{3N} A_j \sum_J^{N_{cell}} \frac{\partial^2 U}{\partial R_{i,I} \partial R_{j,J}} \Big|_{\{R_{i,I}^0\}} \frac{1}{\sqrt{M_i M_j}} e^{ik(R_J - R_I)} \quad (55)$$

It does not matter which Bravais lattice is chosen as a reference point. Therefore, R_I can be taken as zero

$$w^2 A_i = \sum_j^{3N} A_j \sum_J^{N_{cell}} \frac{\partial^2 U}{\partial R_{i,0} \partial R_{j,J}} \Big|_{\{R_{i,0}^0\}} \frac{1}{\sqrt{M_i M_j}} e^{ikR_J} = \sum_j^{3N} A_j D_{ij}(\mathbf{k}) \quad (56)$$

or in a more compact form

$$w^2 \mathbf{a} = \mathbf{D}(\mathbf{k}) \mathbf{a}. \quad (57)$$

$\mathbf{D}(\mathbf{k})$ is called dynamical matrix and it is a square matrix with a size of 3 times the number of atoms in primitive cell throughout this study. Since it is possible to represent the periodicity of crystal with larger cells, it is also possible to define larger matrices. For FCC and BCC elements, the size of the dynamical matrix is 3×3 and for HCP it is 6×6 since there exist 2 atoms in the primitive cell of HCP and 1 atom in the BCC & FCC cells. Equation (57) is an eigenvalue problem and square of the natural frequencies are eigenvalues of the dynamical matrix. In other words, at each \mathbf{k} point in the first Brillouin zone, there exist n natural frequencies, each of which is equal to the square root of an eigenvalue of the dynamical matrix. Phonon dispersion relations can easily be calculated once the dynamical matrices are known and if the phonon dispersion relations are known, Equation (44) can be used to calculate the partition function and the thermodynamic properties. Dynamically unstable phases exhibit negative eigenvalues and the frequencies are imaginary. Phonon frequencies cannot be negative, they are either positive or imaginary. However, imaginary frequencies are conventionally plotted as negative numbers.

It is not possible to calculate harmonic partition function of a dynamically unstable phase. The set of force constants needs to modified and for that purpose, 3 different models are discussed in the following sections.

2.2.1 Double-well Potential

This model stabilizes the soft phonon modes by an approach in which the restoring forces are calculated by a finite displacement of magnitude comparable to the temperature of interest [16]. To describe the soft phonon branch, the proposed double well of the form is [9]

$$U(x) = \frac{1}{2}m\omega_0^2x^2 + \epsilon \left(e^{-x^2/2\sigma^2} - 1 \right), \quad (58)$$

where ω_0 , ϵ , σ are wave vector \mathbf{k} dependent variables.

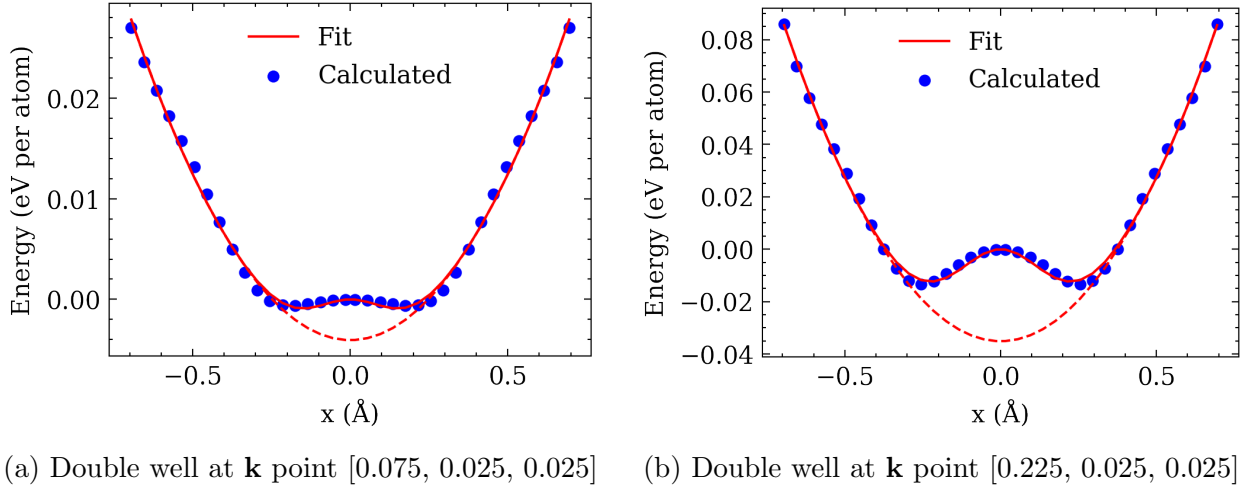


Figure 13: Double-well potentials of BCC Zr. Red lines show the best fit of Equation (58) and dashed lines show the ideal harmonic wells.

A double-well is constructed with a local maximum in the middle for each \mathbf{k} point in reciprocal space in which imaginary frequencies are observed. Figure 13 shows 2 of these \mathbf{k} points as an example. Double-wells are constructed by potentials provided by Ackland and Mendelev [17] and a total of 18 phonon calculations are done with finite displacements of 0.015, 0.055, 0.095 ... Å. Equation (58) is approximately quadratic in high and low energy limits. In order to keep harmonic model valid, it is assumed that phonons reside in an harmonic

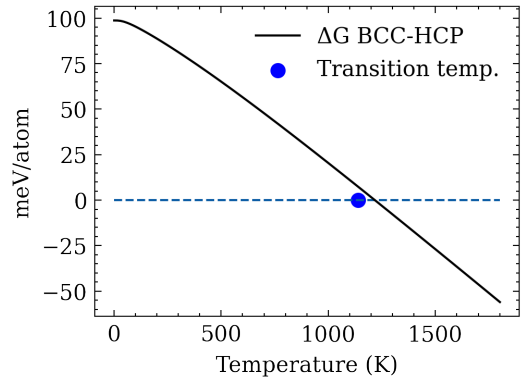


Figure 14: Gibbs energy difference between BCC and HCP Zr.

well (dashed lines in Figure 13) and imaginary frequencies are replaced with fitted ω_0 variables. This kind of approximation allows to construct a $F(V, T)$ surface for dynamically unstable BCC Zr phase and transformation temperature can be estimated. Figure 14 shows the free energy difference between BCC and HCP Zirconium. Even though the results are satisfactory for this set of Zr potentials, it is observed that the Equation (58) does not always fit well. Therefore, the model is not applicable to all phases and additionally, it is only a simplification of anharmonicity.

2.2.2 Temperature Dependent Effective Potential

Similar to the double-well model, temperature dependent effective potential (TDEP) model[18] approximates a harmonic model to the system. Forces and displacements obtained by a molecular dynamics run at any given temperature are used for fitting the force constant matrix. It is possible to construct a dynamically stable harmonic model and thermodynamic integration can be implemented thereafter. The fit of the force constant matrix is done with ordinary least-squares method by using ALM[19] package. Figure 15 shows the

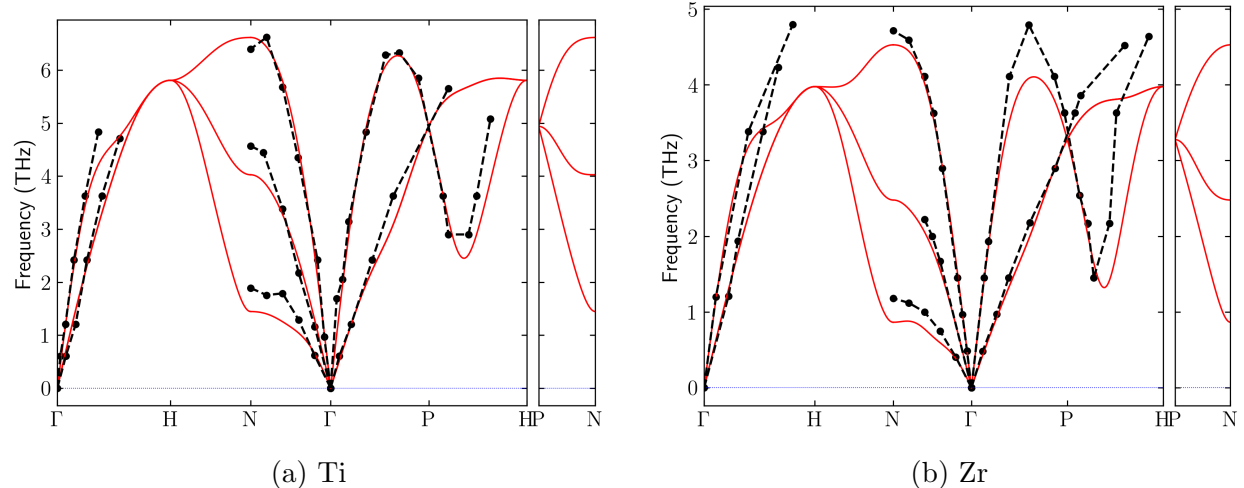


Figure 15: Experimental and calculated phonon dispersion relations of BCC Zr and Ti. Experimental values of Zr[20] and Ti[21] are represented as black dots and the dashed lines between them are for the eye.

calculated versus experimental phonon dispersion relations for BCC Ti and Zr phases. For Ti, interatomic MEAM potentials[22] provided by Won-Seok Ko et al. is used and for Zr, the

same interatomic potential as in the previous double well model is employed. A Langevin dynamics simulation at 1300 K is run for both elements. Calculated frequencies show a good agreement with the experimental values and since fitted force constants are dynamically stable, they can be used for the reference quasi-harmonic model of thermodynamic integration.

2.2.3 High Displacement Model

The default value of finite displacement used for calculation of force constant tensor is 0.01 Å in pyiron. However, double-well potential model shows that the phase can be stabilized by using higher displacements. Figure 16 shows phonon dispersion relations of BCC Ti

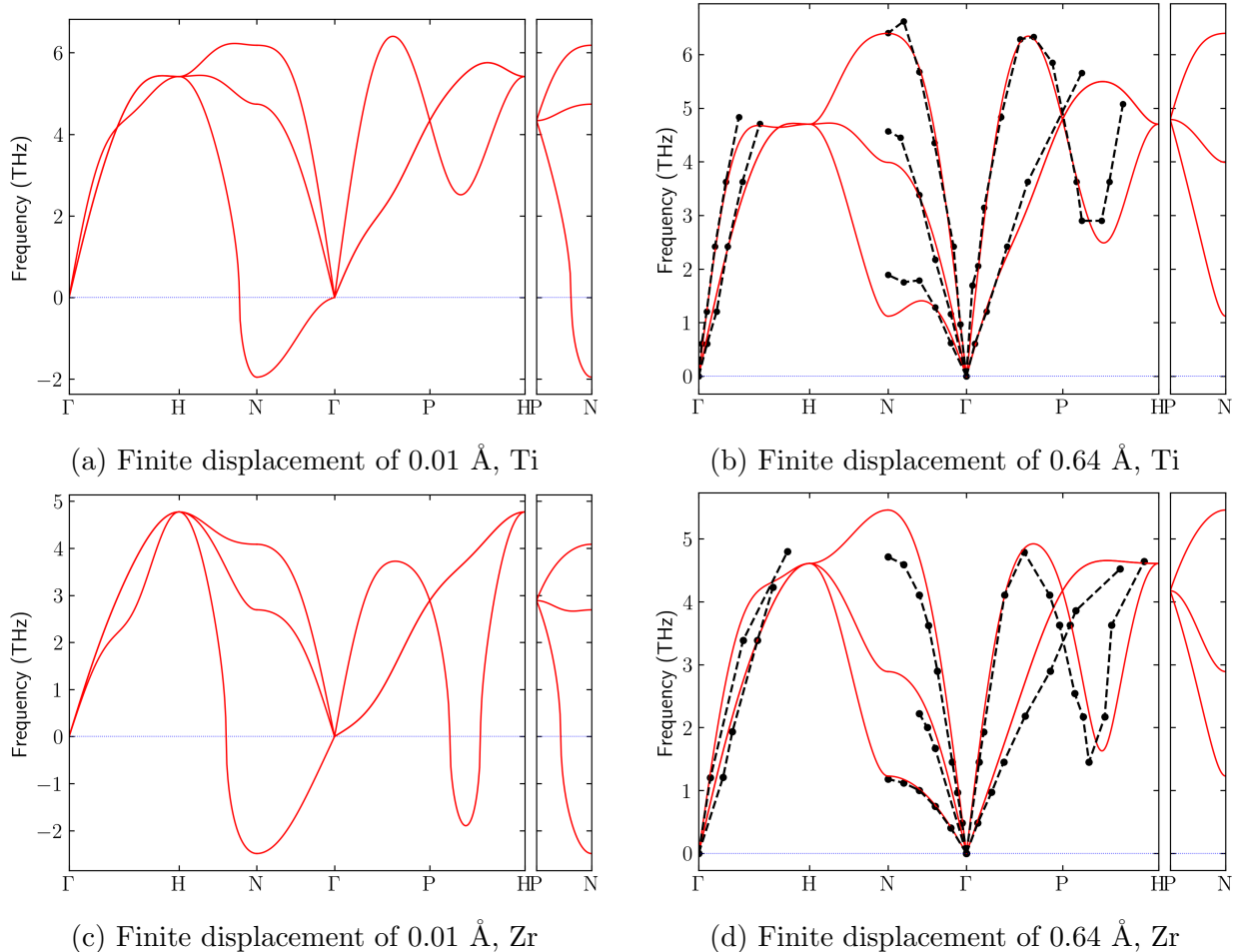


Figure 16: Phonon band structures of BCC Ti and Zr calculated with different finite displacements.

and Zr calculated with two different finite displacements. High displacement model not only stabilizes the phase but also shows good agreement with the experimentally observed frequencies. There is no specific reason for selecting 0.64 Å. Other values such as 1 Å do not show good agreement with the experimental values. However, this has little to no importance on the final result since TI result should not depend on it. In the following chapters, it is shown that the TI result of BCC Ti and Zr are the same for 0.64 and 0.9 Å displacements.

2.3 Heat Capacity

Once the Gibbs free energy surface $G(P, T)$ is known, isobaric heat capacity can be calculated using the relation

$$C_P(T) = -T \left[\frac{\partial^2 G(P, T)}{\partial T^2} \right]_P. \quad (59)$$

Since TI *estimates* or *approximates* the free energy, one needs to take the second derivative of a function defined by noisy data points. This is a notorious problem in applied sciences [23] and inductive bias might lead to misleading results. Therefore an alternative model is derived and used for estimating anharmonic heat capacities.

The probability of observing a microstate x in a canonical ensemble is

$$p(x) = \frac{1}{Z} \exp \left(-\frac{U(x)}{kT} \right). \quad (60)$$

where: $U(x)$ is the total internal energy at microstate x .

The heat capacity at constant volume can be written as

$$\frac{d\langle U \rangle_{p(x)}}{dT} = C_v \quad (61)$$

The expected value of the internal energy is

$$\langle U(x) \rangle_{p(x)} = \int \frac{U(x)}{Z} \exp \left(-\frac{U(x)}{kT} \right) dx. \quad (62)$$

Combining Equation (61) and Equation (62) will yield

$$\begin{aligned} C_v &= \int \frac{\partial}{\partial T} \left(\frac{U(x)}{Z} \exp \left(-\frac{U(x)}{kT} \right) \right) dx \\ &= \int -\frac{\partial Z}{\partial T} \frac{U(x)}{Z^2} \exp \left(-\frac{U(x)}{kT} \right) dx + \int \frac{U(x)}{Z} \exp \left(-\frac{U(x)}{kT} \right) \frac{U(x)}{kT^2} dx. \end{aligned} \quad (63)$$

The partial derivative of partition function Z with respect to temperature T can be written as

$$\begin{aligned} \frac{\partial Z}{\partial T} &= \frac{\partial}{\partial T} \int \exp \left(-\frac{U(x)}{kT} \right) dx \\ &= \int \frac{U(x)}{kT^2} \exp \left(-\frac{U(x)}{kT} \right) dx \\ &= \frac{Z}{kT^2} \int \frac{U(x)}{Z} \exp \left(-\frac{U(x)}{kT} \right) dx, \end{aligned} \quad (64)$$

which is also equal to

$$\frac{\partial Z}{\partial T} = \frac{Z}{kT^2} \langle U \rangle_{p(x)}. \quad (65)$$

Re-writing Equation (63) with Equation (65) will yield

$$C_v = \frac{-Z}{kT^2} \langle U \rangle_{p(x)} \frac{\langle U \rangle_{p(x)}}{Z} + \frac{\langle U^2 \rangle_{p(x)}}{kT^2}, \quad (66)$$

$$C_v = \frac{\langle U^2 \rangle_{p(x)} - \langle U \rangle_{p(x)}^2}{kT^2}. \quad (67)$$

Similar to Equation (60), the probability of observing a microstate x in a NPT ensemble is

$$p(x) = \frac{1}{Z} \exp \left(-\frac{H(x)}{kT} \right), \quad (68)$$

where: $H(x)$ is the enthalpy at microstate x .

And similar to Equation (61), isobaric heat capacity can be written as

$$\frac{d\langle H \rangle_{p(x)}}{dT} = C_p. \quad (69)$$

Same derivation can be done to show that

$$C_p = \frac{\langle H^2 \rangle_{p(x)} - \langle H \rangle_{p(x)}^2}{kT^2}. \quad (70)$$

Within the boundaries of classical mechanics, one can approximate C_p by taking the variance of enthalpies sampled from an NPT ensemble. The heat capacities provided in the following sections are calculated by using the Equation (70).

2.4 Electronic Entropy

Electron's probabilistic occupation of the energy states will contribute to the free energy. This contribution can be significant especially for transition metals and needs to be taken into consideration. A detailed study of electronic contributions is out of scope of this thesis. However, a simple and naive approach is implemented here in order to get a grasp on the order of magnitudes.

Assuming that each energy state x is occupied with a probability of p_x , entropy can be written as

$$S = -k \sum_x n_x (p_x \ln p_x + (1 - p_x) \ln (1 - p_x)). \quad (71)$$

For a set of continuous energy states, summation will turn into an integral

$$S = -k \int n(x) [p(x) \ln p(x) + (1 - p(x)) \ln(1 - p(x))] dx, \quad (72)$$

where: $n(x)$ is the electronic density of states of the crystal.

Applying Fermi statistics to electrons, the probability of occupation at energy state E and temperature T can be written as

$$p(E) = \frac{1}{e^{(E-E_F)/k_B T+1}}, \quad (73)$$

where: E_F is the Fermi energy.

Once the electronic entropy is known, electronic heat capacity at constant volume can be calculated using the relation

$$C_V(T) = T \left(\frac{\partial S}{\partial T} \right)_{T,V}. \quad (74)$$

Electron density of states are taken from Materials Project[24] and calculations are done for T=0 K ideal lattice positions. Figure [17] shows the calculated heat capacities contributions at constant volume for Cu, Ca and Zr. More sophisticated models such as ab initio molecular dynamics simulations[25] that take into account the lattice vibrations are required for more accurate results.

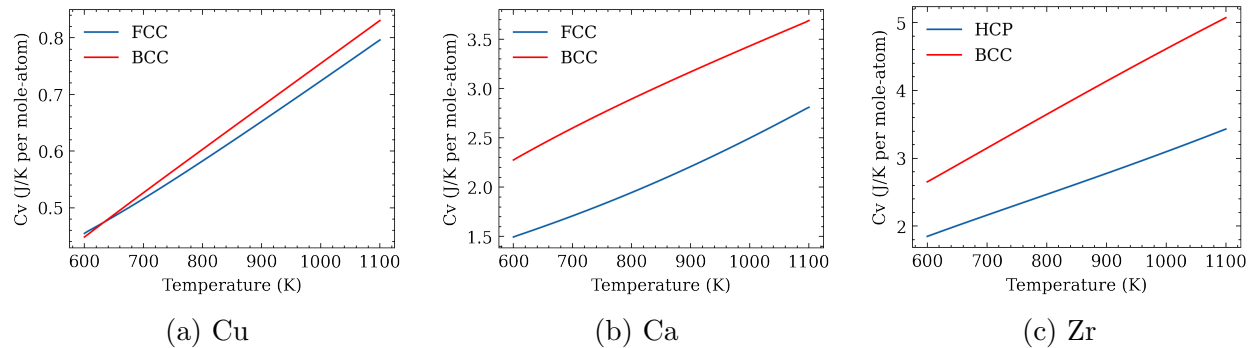


Figure 17: Electronic contributions to the heat capacities.

Electronic free energies are evaluated with the common approximation:

$$F_{el}(T) \approx -\frac{1}{2}TS_{el}(T). \quad (75)$$

3 Results & Discussion

3.1 Titanium

Titanium has HCP crystal structure under the standard reference conditions and transforms into BCC at 1155 K. Due to its technological importance and dynamically unstable BCC phase (Figure 16a), the element is chosen for simulations. In order to show that anharmonic free energy approximation of the BCC phase does not depend on the selected force constants, TILD calculations are performed with 3 different set of force constants. First set of force constants is generated by finite displacement method with a displacement of 0.64 Å and second set is generated with 0.9 Å. Third set is generated by TDEP model. 2000 microstates are sampled using Langevin dynamics for each volume at 1300K and a force constant matrix is fitted. Four Helmholtz free energy $F(V,T)$ surfaces are generated in total, three for BCC and one for HCP phase. Each surface is constructed by performing TILD at 5 different volumes and at 7 different temperatures. The temperatures cover the range from 900

K to 1500 K with 100 K intervals.

128 atom supercells are used for both BCC and HCP phase. Calculations are performed at 12 λ points. Total number of samples at each λ point is 9500 and errors of the means are less than 1meV. Throughout the simulations, MEAM potentials[22] provided by

Won-Seok Ko et al. is used. Figure 18 shows the anharmonic Gibbs free energy difference between BCC and HCP phases. Figure 19

shows the integrands of HCP phase and BCC phase with different set of force constants. As explained in the Theory section, even though the integrals are quite different, approximated

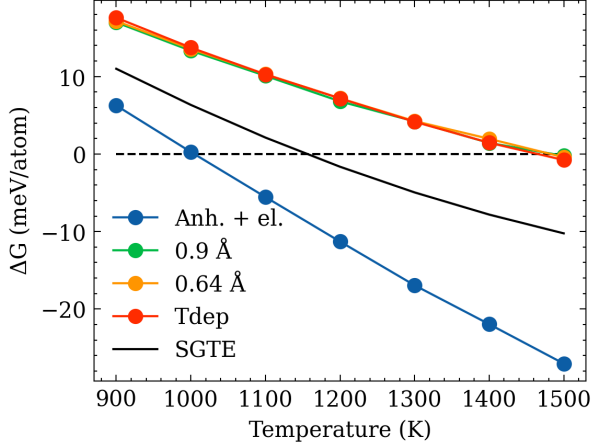


Figure 18: Gibbs energy difference between BCC and HCP Ti.

anharmonic free energies are the same. The transition temperature is overestimated by around 350 K. Adding electronic contributions shifts it from 1500 K to 1000 K and induces 150 K underestimation. Small changes in the free energy curves can lead to significant shifts of transformation temperature. Therefore, an accurate estimation requires the knowledge of all contributions in detail.

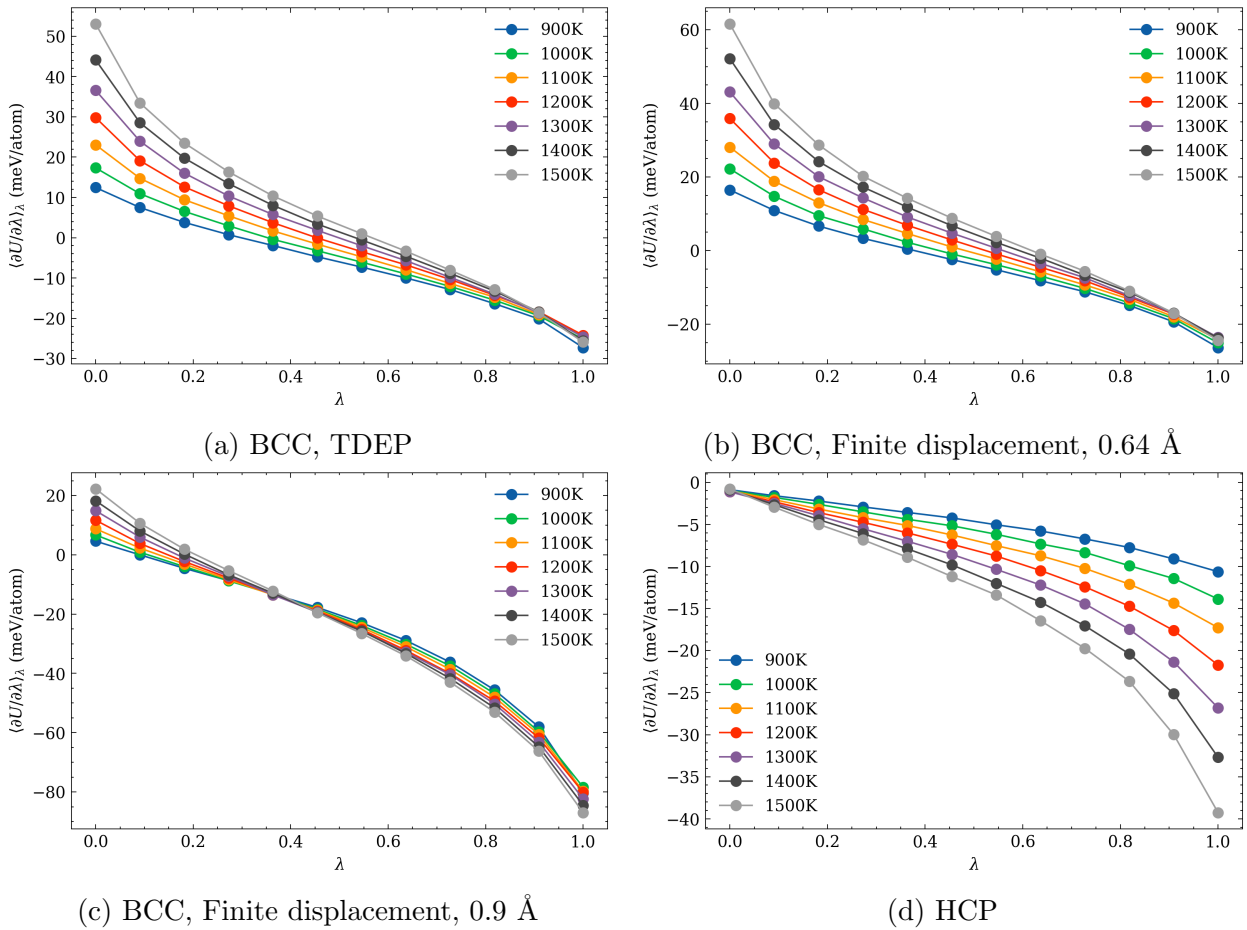


Figure 19: Integrands of Titanium.

Entropies derived from the anharmonic free energies are presented in Figure 20. Derivatives are taken using second order accurate central differences in the interior points and second order accurate one-side differences at the boundaries of the free energy curves. It is observed that vibrational entropies are underestimating the calphad values. Electronic contribution is not negligible in transition metals and the difference is largely due to electronic entropy. Adding electronic contribution yields slightly overestimated entropies for the BCC

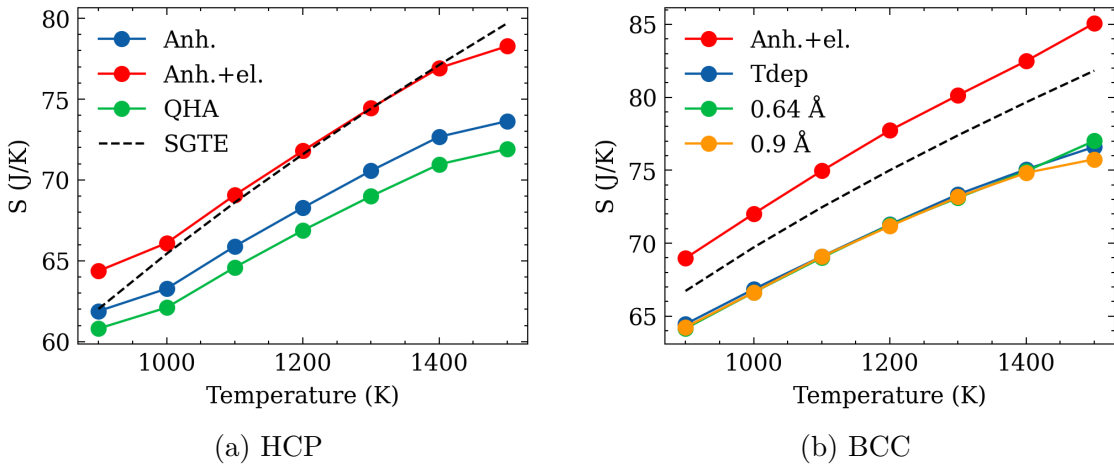


Figure 20: Anharmonic and electronic entropies of titanium.

phase. This might be due to the lack of accuracy of fixed volume fixed density-of-states approximation or the potential. Enthalpy and entropy of transformation are frequently used in calphad assessments and measurement uncertainties are estimated to be small for titanium [26, 27]. Figure 21 shows the entropy and enthalpy difference in vicinity of transformation temperature. Figure 21a shows that the combination of anharmonic and electronic entropies significantly overestimates the experimental value. Similar to the results provided here, Eriksson et al. reports electronic ΔS as 2.25 J/K per mole-atom and anharmonic ΔS as 2.41 J/K per mole-atom where the combination exceeds the experimental value by 1.08 J/K per mole-atom [28]. Zhang et al. reports that electronic free energy difference between BCC and HCP phases is 35 meV/atom at 1500 K [25]. Zhang et al. also reports that different models (static and MD) yield significantly different electronic free energies of BCC W and Nb. As Figure 20b suggests, this might also be the case for BCC Ti.

Calculation of the heat capacity requires the second derivative of the free energy curve and it is very sensitive to fluctuations of approximated free energies. Fitting a smooth curve is not preferred in this study because the results will depend highly on the selected function and this will bring inductive bias. Thus, heat capacities are calculated independently from the TILD results. Figure 22a shows the heat capacities calculated by taking derivatives of TILD free energies using finite difference. Figure 22b shows the heat capacities calculated by the model explained in the Theory section. Nose/Hoover temperature thermostat and

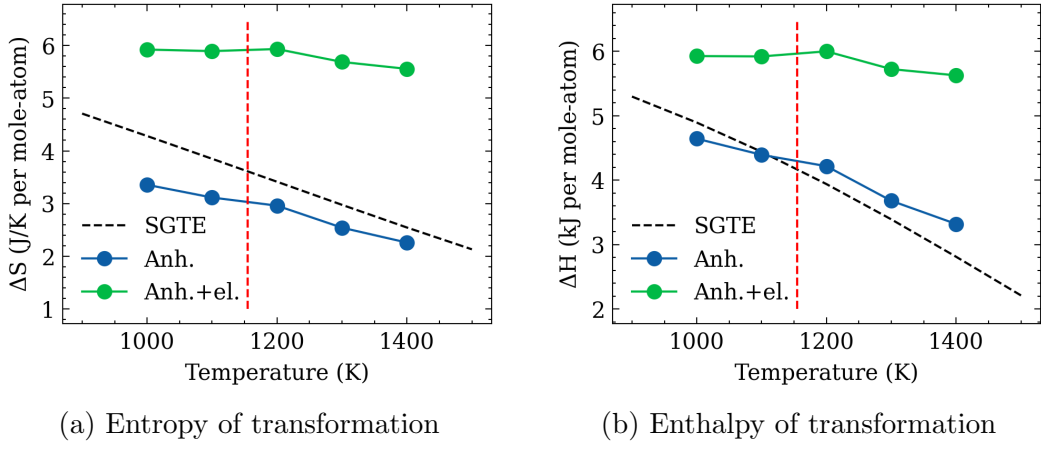


Figure 21: Enthalpy and entropy of transformation. Red dashed line shows the transformation temperature.

Nose/Hoover pressure barostat are used for simulating NPT ensemble and a total of 25000 microstates are sampled. In both cases, electronic contribution to the heat capacity is added to the anharmonic heat capacity. In order to show that the model is not applicable at low temperatures, heat capacity is also approximated at 50 K. The result is close to $3R$ (24.94 J/K per mole-atom) as Dulong-Petit rule suggests. It should be emphasized that the assessment of the accuracy of the model is not straightforward due to many factors, including the limitations of the electronic contribution model, neglected defects, NPT sampling and the quality of selected potentials.

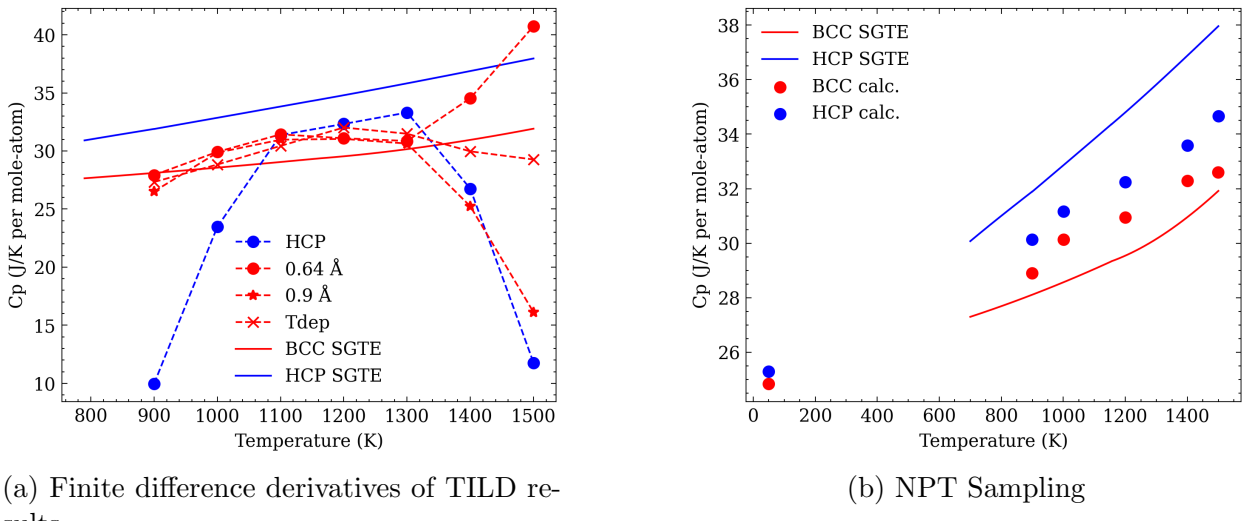


Figure 22: Heat capacity of titanium.

3.2 Zirconium

Similar to titanium, zirconium has HCP crystal structure under the standard reference conditions and transforms into BCC at 1139 K. The applied procedure is the same as titanium. Finnis-Sinclair potential developed by Mendelev and Ackland^[17] is used throughout the simulations. Even though the potential is suitable for the simulation of plastic deformation in the HCP zirconium, there exists another potential in the paper for BCC simulations. Thus, a high accuracy is not expected for the BCC phase. Figure [23] shows the integrands and Figure [24a] shows the Gibbs free energy difference between BCC and HCP phases. Heat capacities are provided in Figure [24b]. Entropies derived from the anharmonic free energies are presented in Figure [25]. Figure [26] shows the enthalpy and entropy of transformation.

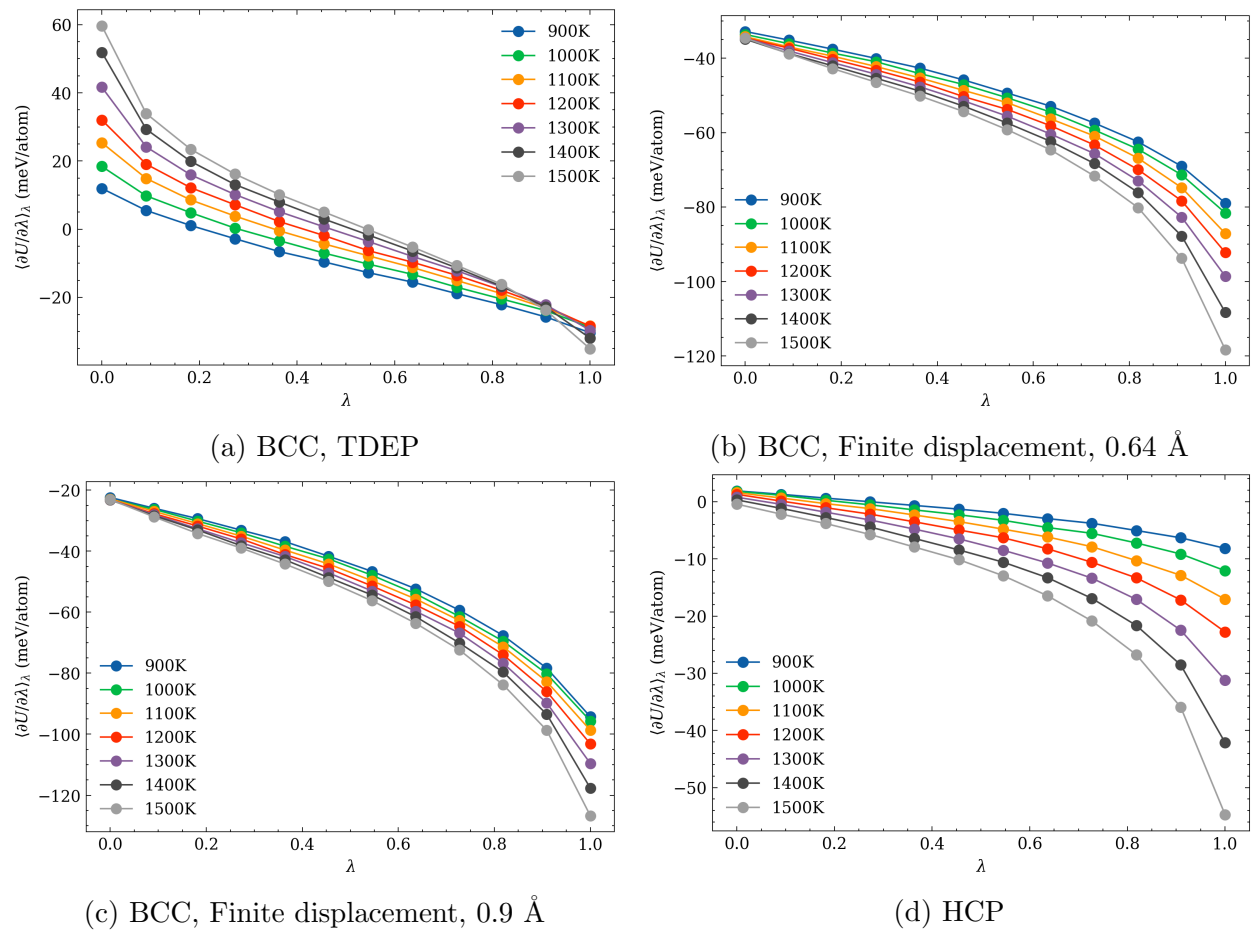
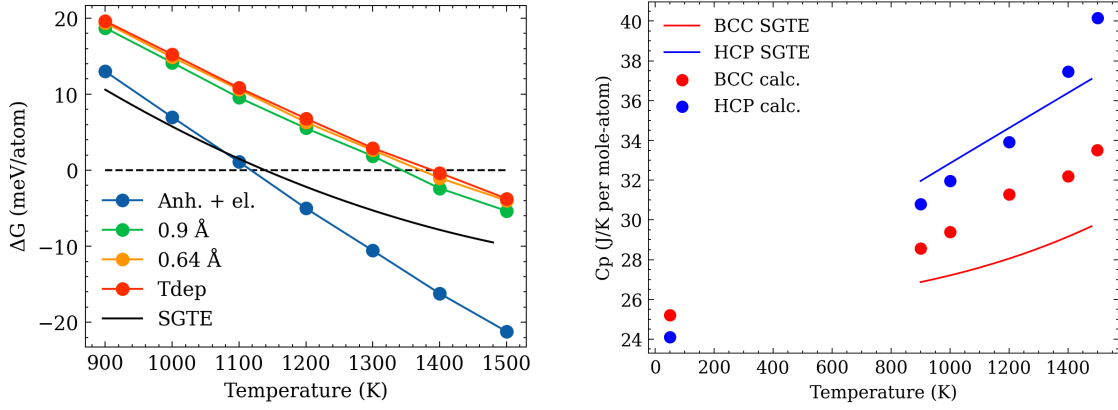


Figure 23: Integrands of Zirconium.



(a) Gibbs energy difference between BCC and HCP Zr.

(b) Heat capacity of Zr.

Figure 24: Free energies and heat capacities of zirconium.

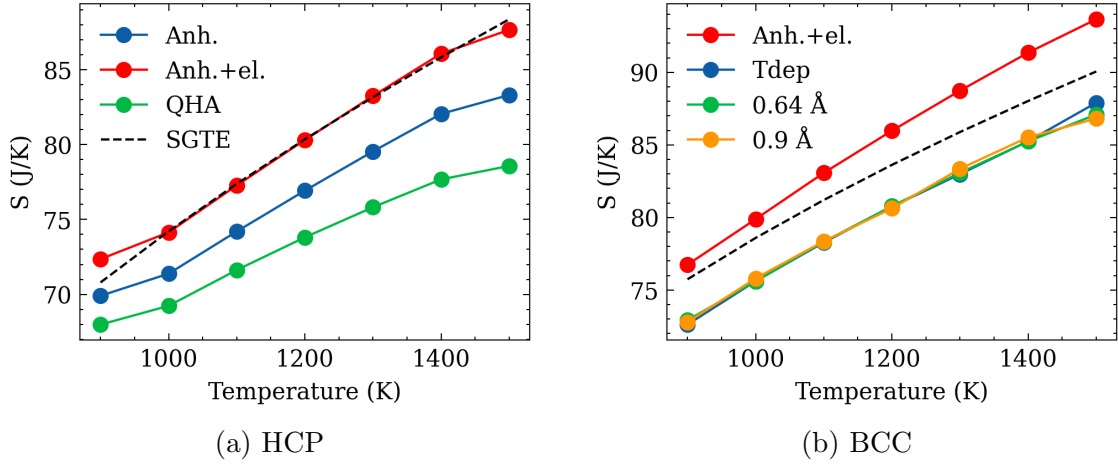


Figure 25: Anharmonic and electronic entropies of zirconium.

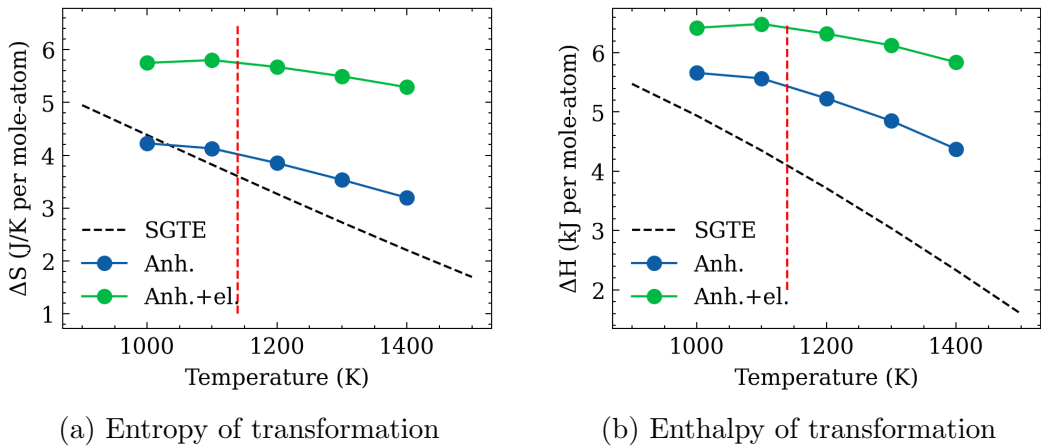


Figure 26: Enthalpy and entropy of transformation. Red dashed line shows the transformation temperature.

Even though the transformation temperature is accurately estimated for zirconium (Figure 24a), entropy and enthalpy of transformation are yielding relatively poor results. Experimental uncertainty is expected to be small for these parameters[29, 30]. Thus, the fortunate estimation of the transformation temperature is not enough to conclude that a simulation is successful. Similar to other simulations, primary reasons for the error might be the quality of the potentials, fixed volume fixed density electronic entropy model and the lack of information available (i.e. defects).

3.3 Calcium

There exists two different set of experimental results for the heat capacity of BCC calcium in the literature. Grabowski et al. have shown that SGTE unary dataset is not the correct one according to the DFT calculations[12]. It is shown that heat capacities calculated by empirical potentials are also in agreement with the DFT results and do not favour the SGTE selection. Morse potential provided by Girifalco and Weizer[31] is used throughout the simulations. Figure 27 shows the calculated versus experimental heat capacities of FCC and BCC calcium. Calculated values are in agreement with the heat capacity curve adopted by Alcock et al.[32] while SGTE unary dataset shows significant deviation.

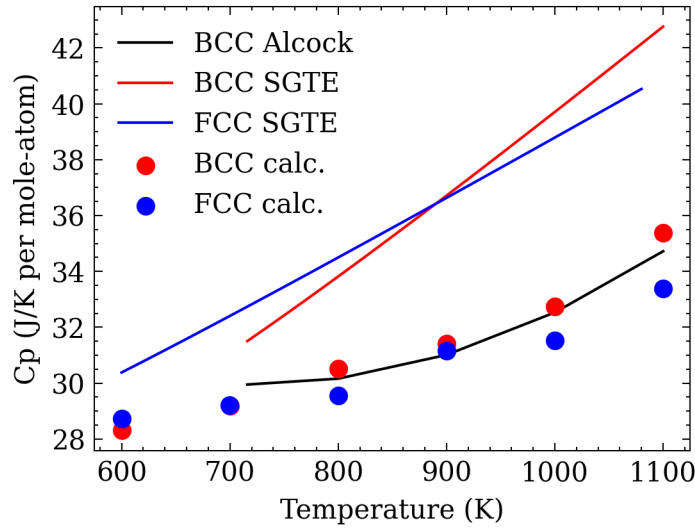


Figure 27: Calculated and experimental heat capacity of calcium.

In addition to heat capacities, Gibbs free energies of the phases are also approximated by

performing TILD and transformation temperature is estimated. The dynamical instability of the BCC phase is prevented by displacing atoms 0.64 \AA and anharmonic Helmholtz free energy $F(V,T)$ surface is constructed by obtaining TILD results at 7 volumes and 9 temperatures. The temperatures cover the range from 600 K to 1000 K with 50 K intervals. 128 and 108 atom supercells are used for BCC and FCC phases respectively. Figure 28 shows the integrands of FCC and BCC structure at different temperatures at the ground state equilibrium volume.

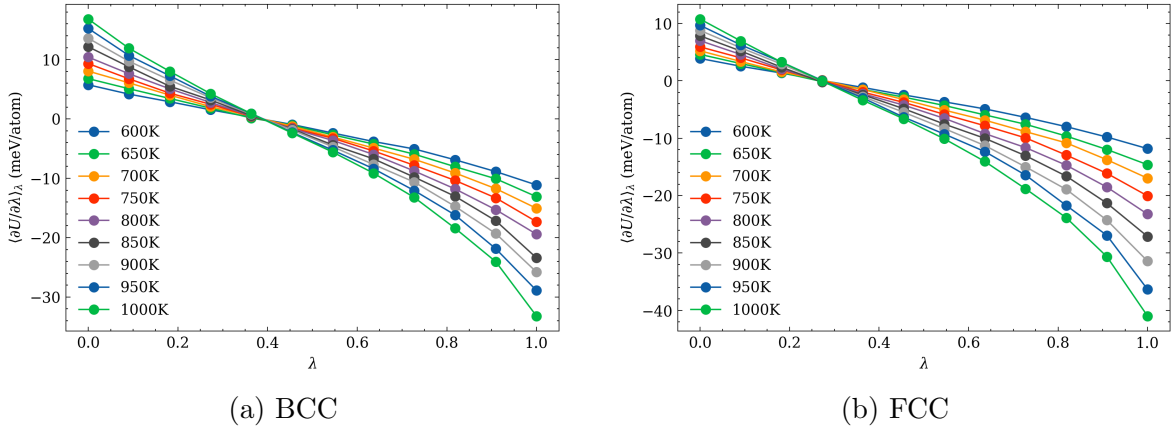


Figure 28: Integrands of Calcium.

The number of lambda points is 12 and the total number of microstates sampled at each lambda point is 5900. Figure 29 shows the anharmonic free energy difference with respect to the temperature. The FCC to BCC transformation temperature is overestimated by around 100 K. Adding electronic contributions reduces it around 200 K. Figure 30 shows the ΔS and ΔH with respect to temperature. Entropies derived from the TILD free energy curves are presented in Figure 31. Derivatives are taken by finite difference method as explained in Titanium section.

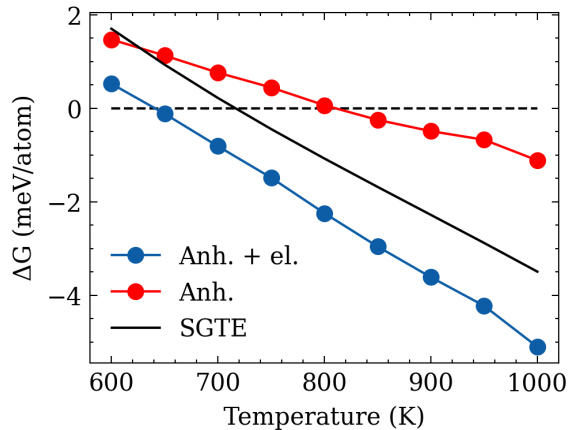


Figure 29: Gibbs energy difference between BCC and FCC Ca.

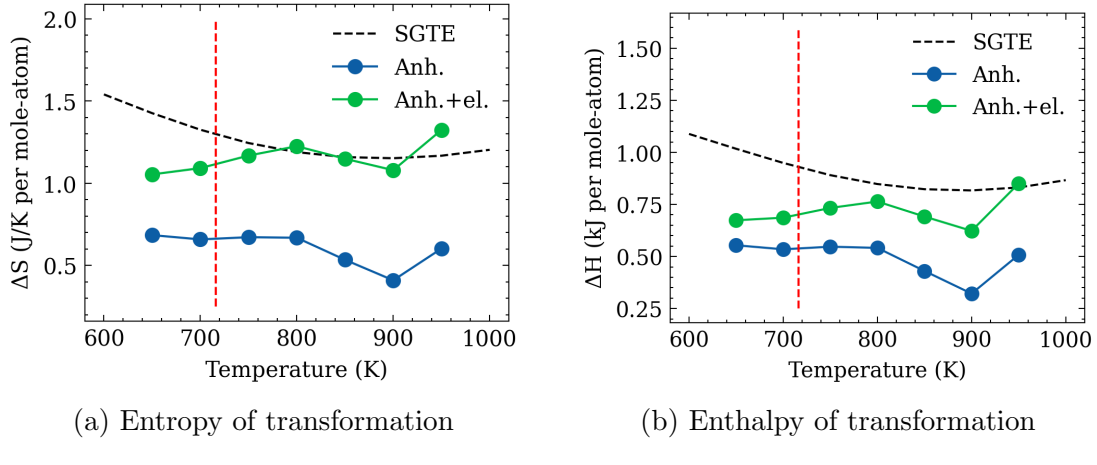


Figure 30: Enthalpy and entropy of transformation. Red dashed line shows the transformation temperature.

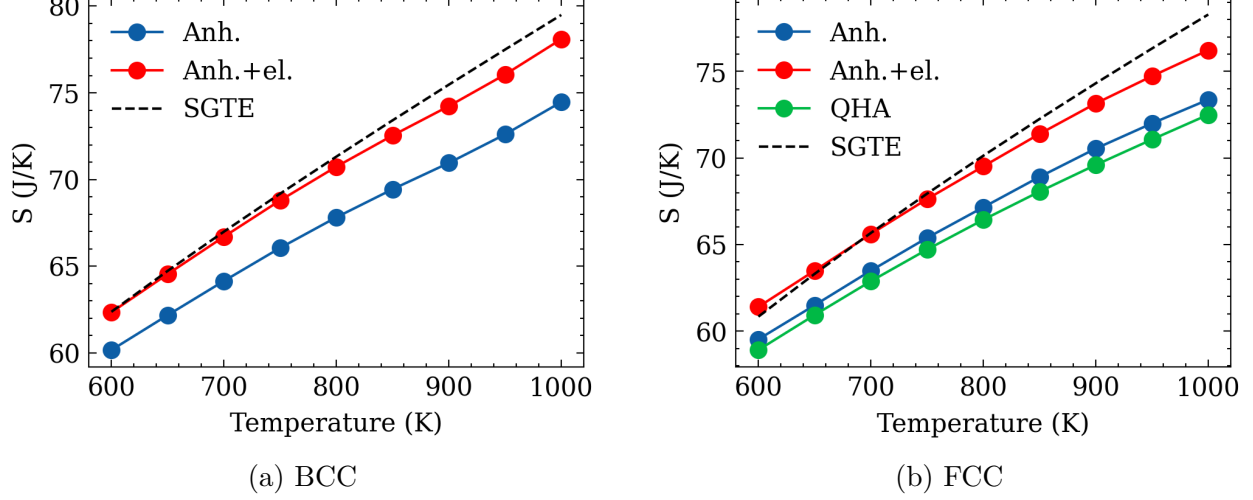


Figure 31: Anharmonic and electronic entropies of calcium.

Impurities play an important role in the allotropic behaviour of calcium[33]. Small amount of hydrogen impurities convert calcium to different phases and unreliable data above 400 K are mostly due to the presence of hydrogen[32]. At high temperatures, the difference between heat capacity measurements are as high as 10 J/K per mole atom. Even though the simulation results are not expected to be very accurate, it is unlikely to have such deviation. Transformation temperature and enthalpy of transformation adopted by Alcock et al. are in agreement with the SGTE dataset. Thus, it is concluded that the overall performance of the simulations is acceptable.

3.4 Al-Cu System

Aluminum-copper alloys have significant importance in industry and the Al-Cu system has been studied as a key binary system for many Al-based and Cu-based alloys[34]. Figure 32 shows the phase diagram of binary Al-Cu system created by FactSage[35] FScopp alloy database. From the the phase diagram it can be inferred that BCC phase is becoming

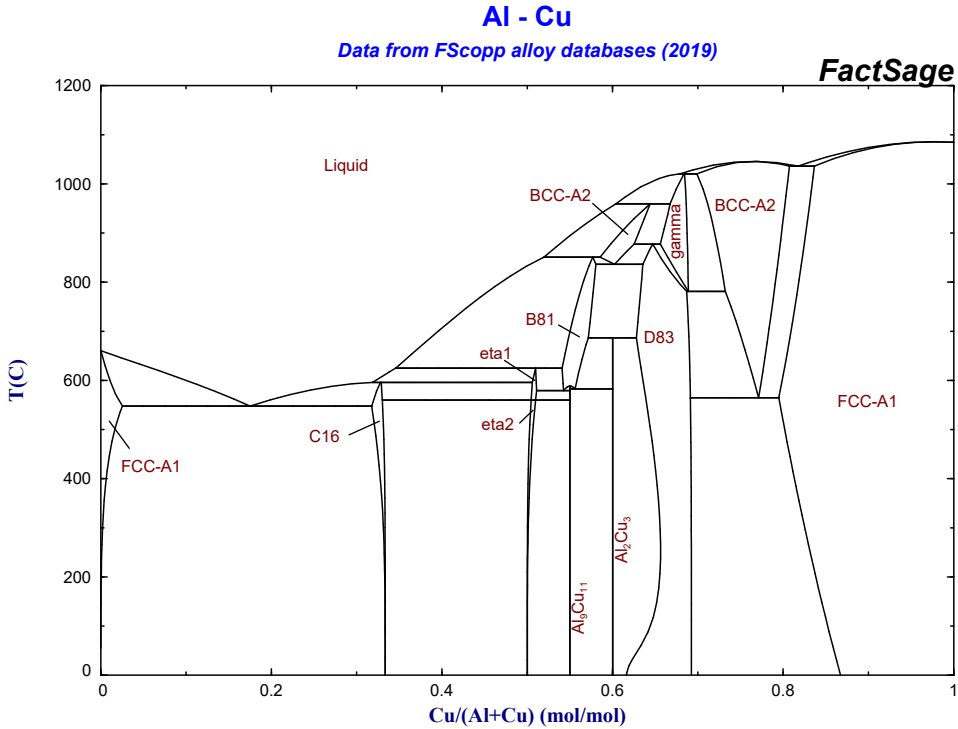


Figure 32: Al-Cu phase diagram from FScopp database.

thermodynamically more favourable than FCC phase at around ~60-80 at.% Cu at elevated temperatures. A phase diagram which consists only of FCC, BCC and liquid phases is also provided in Appendix A. Other phases are not included in the diagram as they fall outside the scope of this study.

BCC solution is dynamically unstable and TILD can be used in order to approximate finite temperature free energies. As the first step of the simulation procedure, 6 supercells are created: 3 BCC cells with 128 atoms and 3 FCC cells with 108 atoms. The compositions of

the cells are 100 at.% Cu, ~90 at.% Cu and ~75 at.% Cu. Supercells other than for pure copper are special quasi-random structures (SQS)[\[36\]](#) created by pyiron. Figure [33](#) shows the supercells.

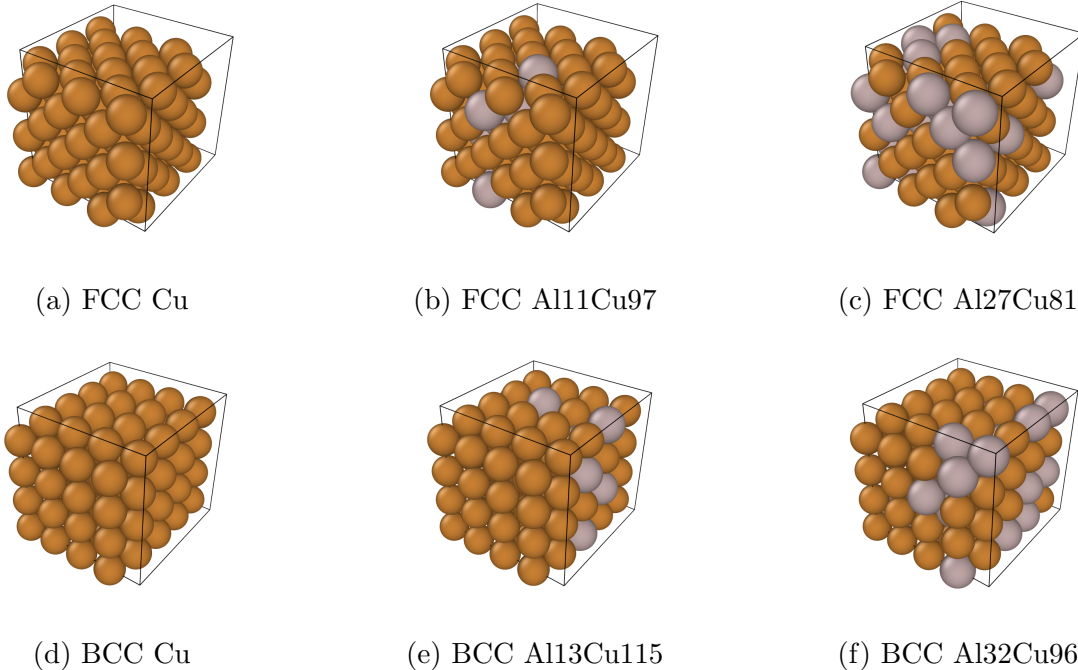


Figure 33: Supercells used for Al-Cu system. Gray spheres represent Al atoms and brown spheres represent Cu atoms.

First, energies of the supercells are calculated for 5 different volumes and Birch-Murnaghan equation of state is fitted at 0 K. Potentials provided by Cai and Ye[\[37\]](#) are used throughout the calculations. As the authors acknowledge, these are simple EAM potentials and are available in the KIM repository. Figure [34](#) shows the equation of state at ground state for 6 supercells. As the Al content increases, equilibrium volume also increases both for BCC and FCC phases. Going from left to right, EOS curves for Cu, Al1Cu9, Al25Cu75 supercells can be observed. The figure yields information about the enthalpy of mixing; however, it is not possible to deduce that increasing Al content will strongly stabilize the BCC phase. FCC is the stable phase for all compositions and the enthalpy difference is 22, 21 and 19 meV per atom for Cu, Al1Cu9 and Al25Cu75 respectively. The corresponding enthalpy differences at room temperature from SGTE dataset are 41.6, 18.9 and 5.3 meV per atom.

Even though the enthalpies deviate significantly, methodology is still capable of predicting the trend (BCC is stabilized over FCC) and to shed light on the stabilization mechanism which may not be dominantly governed by enthalpy of mixing.

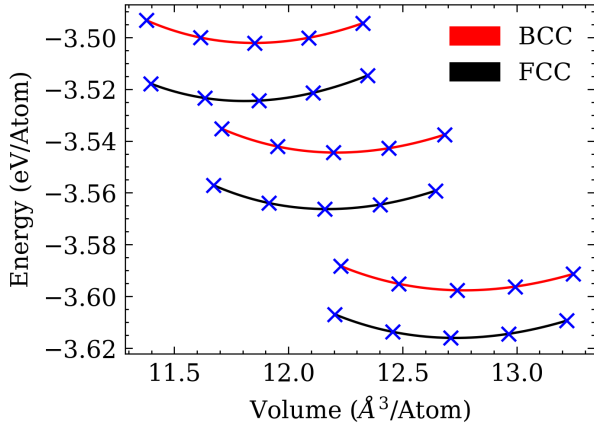
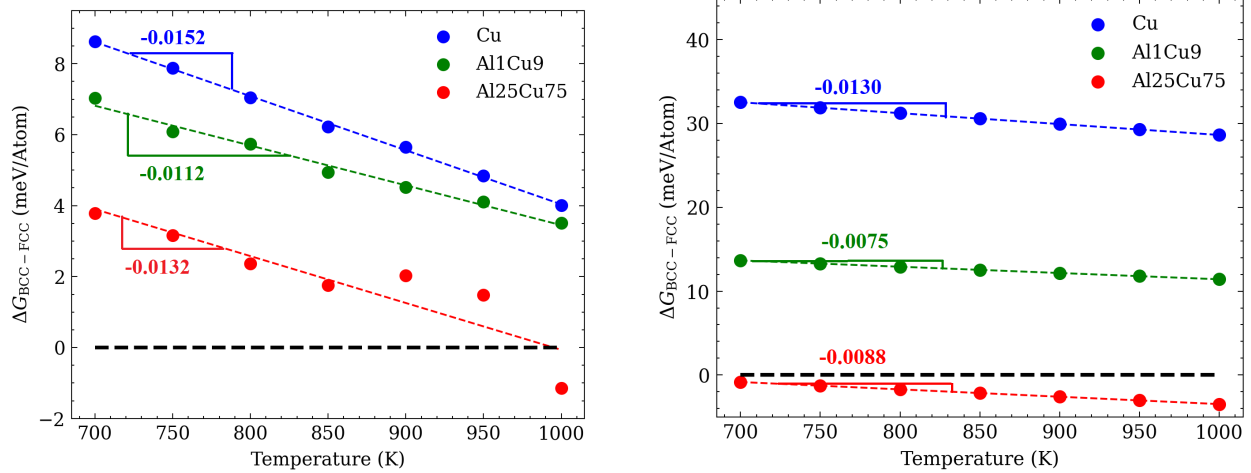


Figure 34: Birch-Murnaghan EOS of the Al-Cu supercells. From left to right, compositions are Cu, Al1Cu9 and Al25Cu75.

Second, $F(V,T)$ surfaces are constructed by performing TILD at 5 different volumes and at 7 different temperatures. The temperatures cover the range from 700 K to 1000 K with 50 K intervals. At higher temperatures, sampling microstates using Langevin dynamics is no more possible. This is highly related with the selected potentials. Figure 39 in Appendix A shows the integrands of different compositions at different temperatures at the ground state equilibrium volume. For pure Cu and Al1Cu9, the number of lambda points is 15 and the total number of microstates sampled at each lambda point is 5960. For Al25Cu75, these numbers are 26 and 3960 respectively. The number of lambda points is increased in order to reduce the weight of slight deviations on the result, especially close to the point $\lambda = 1$. Finally, free energy versus temperature curves are constructed for both phases at different compositions. Figure 35 shows the free energy differences $\Delta G_{\text{BCC-FCC}}$. It shows that increasing the Al content is making the BCC phase thermodynamically more favourable compared to the FCC phase and the transformation temperature is reduced. A more accurate temperature assessment could be achieved by taking the electronic contribution and defects into account and using DFT results instead of empirical potentials, which would however take a considerable amount of time.



(a) Calculated Gibbs energy differences of supercells

(b) Gibbs energy differences in SGTE dataset.

Figure 35: Gibbs energy difference between BCC and FCC solutions at different chemical compositions.

Figure 36 shows the calculated heat capacities for the FCC and BCC phases of pure Al and Cu. Since the electronic contribution is not significant, it is not taken into account. In SGTE dataset, FCC and BCC phases are represented by the same heat capacity function and the approximated results are in agreement with the SGTE unary dataset. Heat capacity of aluminum is slightly overestimated. Above 800 K, BCC aluminum does not stay stable for this set of potential. As a result, heat capacities are not approximated above this temperature.

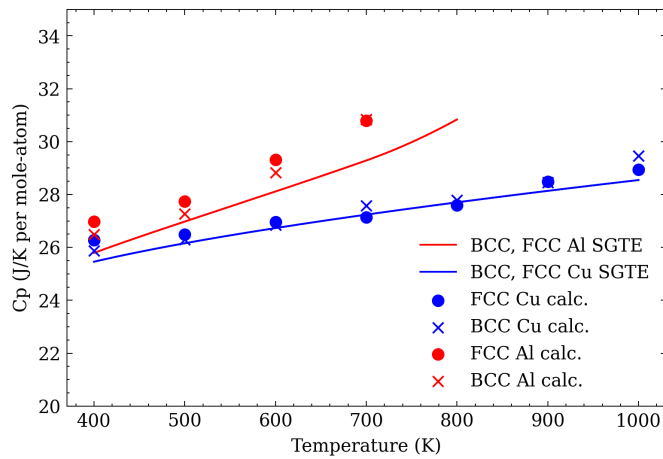
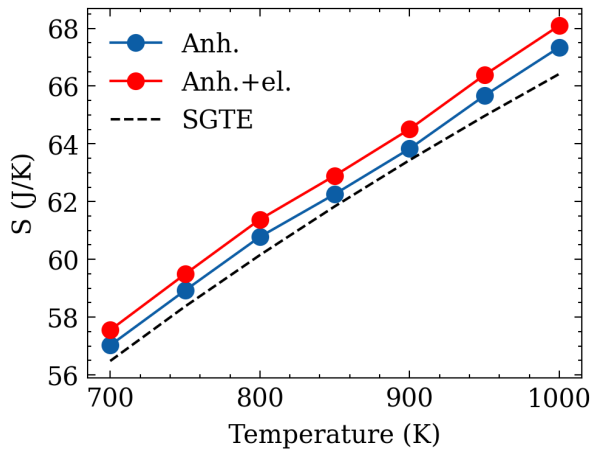
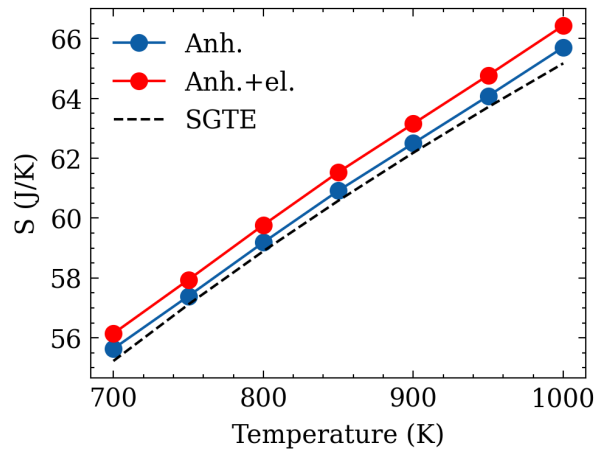


Figure 36: Heat capacities of pure Al and Cu.



(a) BCC



(b) FCC

Figure 37: Anharmonic and electronic entropies of copper.

Figure 37 shows the absolute entropies of FCC and BCC copper. It can be concluded that the agreement with the calphad data is not poor for pure copper, taking into consideration the absolute entropies and heat capacities. However, it should be re-emphasized that the calculated energy of the FCC-BCC stability is twice as large as the corresponding calphad value.

4 Conclusions

In his 1957 essay "Information Theory and Statistical Mechanics" [38], E. T. Jaynes writes "If one considers statistical mechanics as a form of statistical inference rather than as a physical theory, it is found that the usual computational rules, starting with the determination of the partition function, are an immediate consequence of the maximum-entropy principle. In the resulting subjective statistical mechanics, the usual rules are thus justified independently of any physical argument." and he continues, "It is possible to maintain a sharp distinction between statistical mechanics' physical and statistical aspects. The former consists only of the correct enumeration of the states of a system and their properties; the latter is a straightforward example of statistical inference." This thesis is all about the determination of the partition function. And as Jaynes stated, usual rules are independent of any physical argument. Both models—free energy perturbation theory and thermodynamic integration—are merely approximate inference methods and they are not specific to the area of thermodynamics.

Throughout the simulations, randomly selected empirical potentials are used. It is observed that none of them performed very poorly. Primary reason for avoiding DFT calculations is the time requirement. One can fit any sort of potential on DFT results and then can apply a two staged TILD, this is known as TU-TILD[13] method in literature. Adding electronic contributions on anharmonic free energies calculated by empirical potentials is open to discussion. It can be assumed that these potentials are taking electronic contributions into account at some level. Thus, TU-TILD approach might be a better option especially if it is combined with an advanced electronic free energy approximation model.

Free energy approximation of dynamically unstable crystal structures does not require a different TILD model than dynamically stable phases. Results are independent of the proposal distribution and any set of force constants that does not yield imaginary frequencies can be selected as a reference. However, it is more convenient to select a proposal distribution that is similar to the target distribution because this will reduce the number of samples required.

Experimental results such as transition temperature, enthalpy of transformation and entropy of transformation are very sensitive to changes in free energy curves. Only a few meV difference might cause a few hundred Kelvin temperature shifts. Combined with the uncertainty, this makes accurate estimation of these parameters a very hard and challenging task. For instance, 1% change in the absolute entropy of the BCC Ca will cause ΔS value shift around 50%. However, results might be very useful for Calphad modeling especially if the experimental data is scarce or hard to achieve.

5 Declaration of Originality

I hereby declare that, unless stated otherwise, this work is the result of my own efforts. These efforts include the originality of written materials, figures, images and experimental results. Where material is drawn from elsewhere, references are included.

Place, date and signature

Appendices

Appendix A Al-Cu System

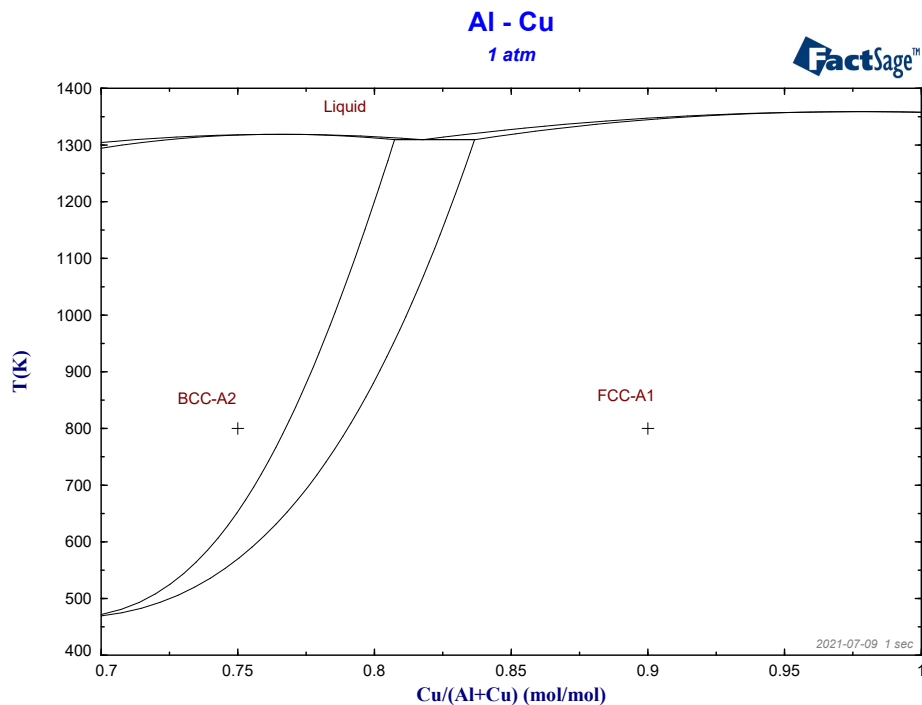


Figure 38: Al-Cu phase diagram with FCC, BCC and liquid phases only.

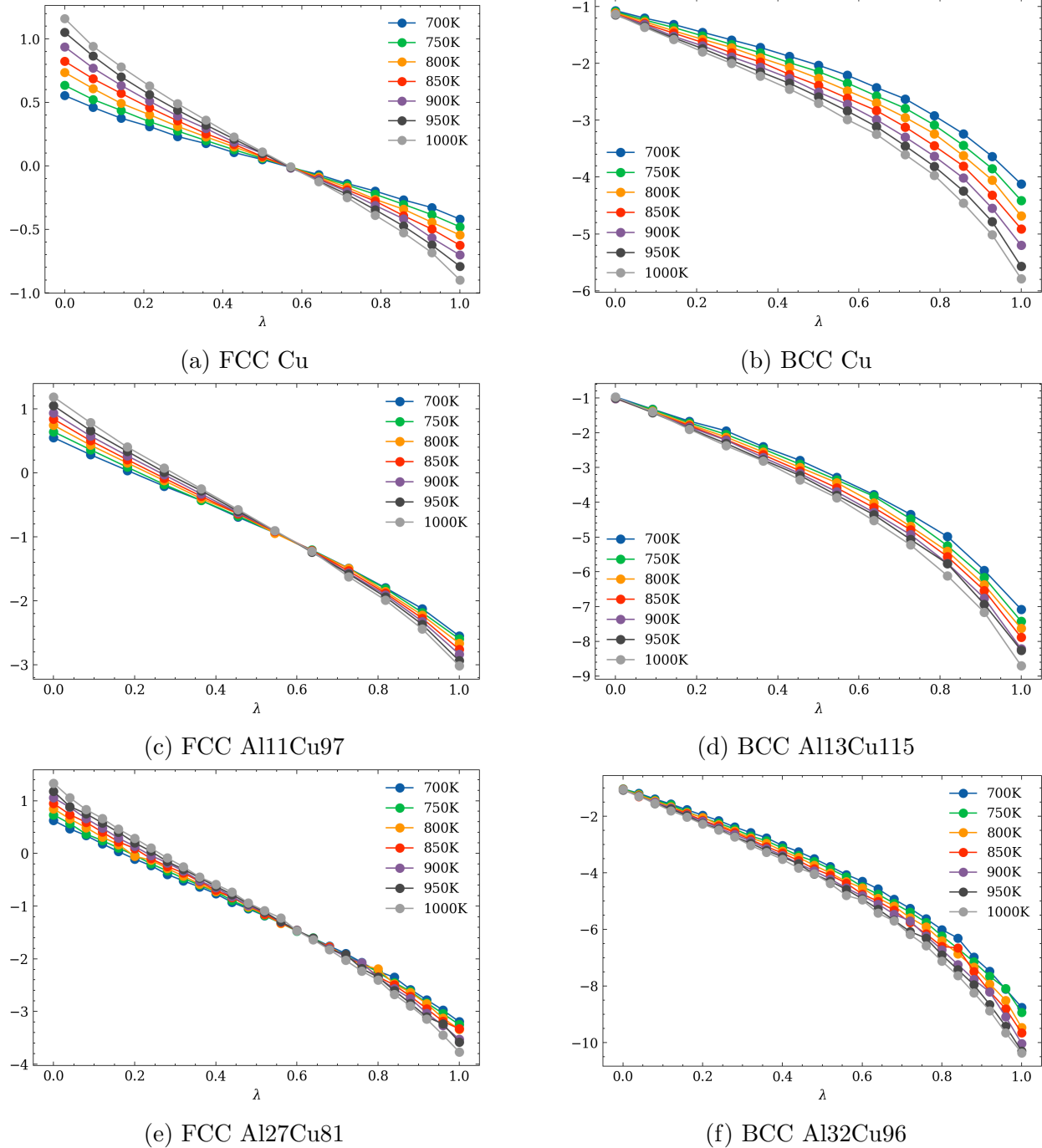


Figure 39: Integrands at ground state equilibrium volume.

References

- [1] G. Petretto, S. Dwaraknath, H. P C Miranda, D. Winston, M. Giantomassi, M. J. van Setten, X. Gonze, K. A. Persson, G. Hautier, and G.-M. Rignanese, “High-throughput density-functional perturbation theory phonons for inorganic materials,” *Scientific data*, vol. 5, 2018.
- [2] A. Togo, “Phonon database at kyoto university.” <http://phonondb.mtl.kyoto-u.ac.jp>.
- [3] S. Kadkhodaei, Q.-J. Hong, and A. van de Walle, “Free energy calculation of mechanically unstable but dynamically stabilized bcc titanium,” *Physical Review B*, vol. 95, no. 6, 2017.
- [4] E. B. Tadmor, R. S. Elliott, J. P. Sethna, R. E. Miller, and C. A. Becker, “The potential of atomistic simulations and the knowledgebase of interatomic models,” *JOM*, vol. 63, no. 7, p. 17, 2011.
- [5] J. Janssen, S. Surendralal, Y. Lysogorskiy, M. Todorova, T. Hickel, R. Drautz, and J. Neugebauer, “pyiron: An integrated development environment for computational materials science,” *Computational Materials Science*, vol. 163, pp. 24–36, 2019.
- [6] S. Plimpton, “Fast parallel algorithms for short-range molecular dynamics,” *Journal of Computational Physics*, vol. 117, no. 1, pp. 1–19, 1995.
- [7] A. Togo and I. Tanaka, “First principles phonon calculations in materials science,” *Scripta Materialia*, vol. 108, pp. 1–5, 2015.
- [8] A. Glensk, B. Grabowski, T. Hickel, and J. Neugebauer, “Understanding anharmonicity in fcc materials: From its origin to ab initio strategies beyond the quasiharmonic approximation,” *Physical review letters*, vol. 114, no. 19, p. 195901, 2015.

- [9] N. D. Drummond and G. J. Ackland, “Ab initio quasiharmonic equations of state for dynamically stabilized soft-mode materials,” *Physical Review B*, vol. 65, no. 18, 2002.
- [10] O. Hellman, I. A. Abrikosov, and S. I. Simak, “Lattice dynamics of anharmonic solids from first principles,” *Physical Review B*, vol. 84, no. 18, 2011.
- [11] B. Grabowski, L. Ismer, T. Hickel, and J. Neugebauer, “Ab initio up to the melting point: Anharmonicity and vacancies in aluminum,” *Physical Review B*, vol. 79, no. 13, 2009.
- [12] B. Grabowski, P. Söderlind, T. Hickel, and J. Neugebauer, “Temperature-driven phase transitions from first principles including all relevant excitations: The fcc-to-bcc transition in ca,” *Physical Review B*, vol. 84, no. 21, 2011.
- [13] A. I. Duff, T. Davey, D. Korbacher, A. Glensk, B. Grabowski, J. Neugebauer, and M. W. Finnis, “Improved method of calculating ab initio high-temperature thermodynamic properties with application to zrc,” *Physical Review B*, vol. 91, no. 21, 2015.
- [14] R. W. Zwanzig, “High-temperature equation of state by a perturbation method. i. nonpolar gases,” *The Journal of Chemical Physics*, vol. 22, no. 8, pp. 1420–1426, 1954.
- [15] Y. Mishin, D. Farkas, M. Mehl, and D. Papaconstantopoulos, “Interatomic potentials for monoatomic metals from experimental data and ab initio calculations,” *Physical Review B*, vol. 59, no. 5, p. 3393, 1999.
- [16] G. Ackland, “Elastic properties as a pointer to phase transitions,” 2000.
- [17] M. I. Mendelev and G. J. Ackland, “Development of an interatomic potential for the simulation of phase transformations in zirconium,” *Philosophical Magazine Letters*, vol. 87, no. 5, pp. 349–359, 2007.
- [18] O. Hellman, P. Steneteg, I. A. Abrikosov, and S. I. Simak, “Temperature dependent effective potential method for accurate free energy calculations of solids,” *Physical Review B*, vol. 87, no. 10, 2013.

- [19] T. Tadano, Y. Gohda, and S. Tsuneyuki, “Anharmonic force constants extracted from first-principles molecular dynamics: applications to heat transfer simulations,” *Journal of Physics: Condensed Matter*, vol. 26, no. 22, p. 225402, 2014.
- [20] Heiming, Petry, Trampenau, Alba, Herzig, Schober, and Vogl, “Phonon dispersion of the bcc phase of group-iv metals. ii. bcc zirconium, a model case of dynamical precursors of martensitic transitions,” *Physical review. B, Condensed matter*, vol. 43, no. 13, pp. 10948–10962, 1991.
- [21] Petry, Heiming, Trampenau, Alba, Herzig, Schober, and Vogl, “Phonon dispersion of the bcc phase of group-iv metals. i. bcc titanium,” *Physical review. B, Condensed matter*, vol. 43, no. 13, pp. 10933–10947, 1991.
- [22] W.-S. Ko, B. Grabowski, and J. Neugebauer, “Development and application of a ni-ti interatomic potential with high predictive accuracy of the martensitic phase transition,” *Physical Review B*, vol. 92, no. 13, 2015.
- [23] I. Knowles and R. J. Renka, “Methods for numerical differentiation of noisy data,” *Electron. J. Differ. Equ.*, vol. 21, pp. 235–246, 2014.
- [24] A. Jain, S. P. Ong, G. Hautier, W. Chen, W. D. Richards, S. Dacek, S. Cholia, D. Gunter, D. Skinner, G. Ceder, and K. A. Persson, “Commentary: The materials project: A materials genome approach to accelerating materials innovation,” *APL Materials*, vol. 1, no. 1, p. 011002, 2013.
- [25] X. Zhang, B. Grabowski, F. Körmann, C. Freysoldt, and J. Neugebauer, “Accurate electronic free energies of the 3d,4d , and 5d transition metals at high temperatures,” *Physical Review B*, vol. 95, no. 16, 2017.
- [26] E. Kaschnitz and P. Reiter, “Enthalpy and temperature of the titanium alpha-beta phase transformation,” *International journal of thermophysics*, vol. 23, no. 5, pp. 1339–1345, 2002.

- [27] A. Cezairliyan and A. Miiller, “Thermodynamic study of the $\alpha \rightarrow \beta$ phase transformation in titanium by a pulse heating method,” *JOURNAL OF RESEARCH of the National Bureau of Standards*, vol. 83, no. 2, 1978.
- [28] O. Eriksson, J. Wills, and D. Wallace, “Electronic, quasiharmonic, and anharmonic entropies of transition metals,” *Physical Review B*, vol. 46, no. 9, p. 5221, 1992.
- [29] A. Cezairliyan and F. Righini, “Thermodynamic studies of the $\alpha \rightarrow \beta$ phase transformation in zirconium using a subsecond pulse heating technique,” *Journal of research of the National Bureau of Standards. Section A, Physics and chemistry*, vol. 79, no. 1, p. 81, 1975.
- [30] F. J. Mompean, J. Perrone, M. Illemassène, *et al.*, “Chemical thermodynamics of zirconium,” 2005.
- [31] L. A. Girifalco and V. G. Weizer, “Application of the morse potential function to cubic metals,” *Physical Review*, vol. 114, no. 3, p. 687, 1959.
- [32] C. Alcock, M. Chase, and V. Itkin, “Thermodynamic properties of the group ia elements,” *Journal of physical and chemical reference data*, vol. 23, no. 3, pp. 385–497, 1994.
- [33] J. Smith and B. Bernstein, “Effects of impurities on the crystallographic modifications of calcium metal,” *Journal of the Electrochemical Society (US) Absorbed Electrochem. Technol.*, vol. 106, 1959.
- [34] A. Kroupa, O. Zobač, and K. W. Richter, “The thermodynamic reassessment of the binary al–cu system,” *Journal of Materials Science*, vol. 56, no. 4, pp. 3430–3443, 2021.
- [35] C. W. Bale, P. Chartrand, S. Degterov, G. Eriksson, K. Hack, R. B. Mahfoud, J. Melançon, A. Pelton, and S. Petersen, “Factsage thermochemical software and databases,” *Calphad*, vol. 26, no. 2, pp. 189–228, 2002.

- [36] A. Zunger, S.-H. Wei, L. Ferreira, and J. E. Bernard, “Special quasirandom structures,” *Physical review letters*, vol. 65, no. 3, p. 353, 1990.
- [37] J. Cai and Y. Ye, “Simple analytical embedded-atom-potential model including a long-range force for fcc metals and their alloys,” *Physical Review B*, vol. 54, no. 12, p. 8398, 1996.
- [38] E. T. Jaynes, “Information theory and statistical mechanics,” *Physical review*, vol. 106, no. 4, p. 620, 1957.